ELECTROMECHANICAL INTERACTIONS IN THE HEART: A COMPUTATIONAL STUDY

By
Yuxuan Hu

A dissertation submitted to Johns Hopkins University in conformity with the requirements for the degree of Doctor of Philosophy

Baltimore, Maryland
March 2014

Abstract

The motivation for this research was to fill gaps in the current understanding of the electromechanical interactions in the heart, with the expectation that this improved understanding will lead to better treatment for cardiac diseases, specifically cardiac arrhythmias and dyssynchronous heart failure (DHF).

This research was conducted using a computer modeling approach, making it possible to analyze the electrical and mechanical activity in the whole heart at a high spatiotemporal resolution. First, it was investigated how the recruitment of stretch-activated channel (SAC) affects scroll wave stability. Second, the predominant mechanism underlying stroke work improvement in the acute response of cardiac resynchronization therapy (CRT) was determined. Third, the feasibility of optimizing CRT pacing locations to achieve maximal hemodynamics improvement while simultaneously minimizing ATP consumption heterogeneity throughout the left ventricle in the DHF ventricles was demonstrated.

Regarding the effects of mechano-electric feedback on arrhythmias, It was found that recruitment of SAC affects scroll wave stability differently depending on SAC reversal potential and channel conductance; the mechanisms are also different. Regarding CRT

therapy for DHF patients, the predominant mechanism underlying stroke work improvement in the acute response of CRT was found to be efficient preloading of the ventricles by a properly timed atrial contraction instead of resynchronization of ventricular contraction. Reduction of mitral regurgitation by CRT led to stroke work worsening. Lastly, an ATP based method to optimize CRT pacing sites was suggested for DHF ventricles.

This research provides insights into the electromechanical interactions in the heart, and will contribute to the development of better treatment for cardiac diseases, specifically cardiac arrhythmias and DHF.

Primary Reader: Dr. Natalia A. Trayanova

Secondary Reader: Dr. Thao Nguyen

To my parents

Acknowledgments

This work will not be possible without the support of my advisor, Dr. Natalia Trayanova. I thank her for the knowledge she generously imparted to me and the resources she provided to maximize my learning experience. I also thank her for the freedom she gave me in exploring my academic interests and taking on different projects.

I thank Dr. Viacheslav Gurev for teaching me cardiac mechanics and providing me with the best cardiac mechanics model for my project.

I thank Dr. Jason Constantino for his help in everything, from polishing academic writings to SBE I homework.

I thank all my lab peers for being my best friends in Baltimore.

Last but not least, I want to thank my parents, especially my mother, for always supporting me, both financially and emotionally. Without their encouragements and belief in my abilities, I would not have gone this far.

Table of Contents

List of Tables

List of Figures

CHAPTER 3:

CHAPTER 4:

APPENDIX A:

List of Abbreviations

APD = action potential duration

ATP_c = ATP consumption per myosin head

ATP_cT = total ATP_c over one pacing cycle

ATPCTHI = ATP_cT heterogeneity index

AV delay = atrioventricular delay

CRT = cardiac resynchronization therapy

CV = conduction velocity

DHF = dyssynchronous heart failure

DTMRI = diffusion tensor magnetic resonance image

ECG = electrocardiogram

HH = Hodgkin and Huxley

LA = left atrium

LBBB = left bundle branch block

LV = left ventricle

MEF = mechano-electric feedback

MRI = magnetic resonance image

RA = right atrium

RV = right ventricle

SAC = stretch-activated channel

SR = sarcoplasmic reticulum

VF = ventricular fibrillation

Chapter 1

Background and Motivation

1.1 The heart

The heart is the pump in the cardiovascular system. The human heart has four chambers: the left atrium (LA), the right atrium (RA), the left ventricle (LV) and the right ventricle (RV). Each has its own unique function. The vena cava delivers deoxygenated blood into the RA and then the blood flows into the RV. The RV pumps the blood through pulmonary artery into the lungs for gaseous exchange so that the blood can be oxygenated. Oxygenated blood returns back into the left side of the heart through pulmonary vein. It first goes into the LA and then into the LV, from which it gets pumped into the circulatory system through aorta. The mechanical pumping action of the heart is controlled by an electrical signal that usually originates from sinoatrial node located in the RA of the heart. The cardiac cycle usually repeats 50 to 120 times per minute in humans.

1.1.1 Electrical signal in the heart

The electrical signal, in sinus rhythm, originates from the sinoatrial node and propagates down the atrium to the atrioventricular node. It then propagates through the Purkinje fibers, into the respective bundle branches and finally excites the ventricular walls. The heart muscle (myocardium) is made up of coupled electrically excitable cells (cardiac myocytes). These cells fire action potentials and are electrically coupled through gap junctions, which provide low resistance for the action potential to propagate between neighboring cells, thus allowing for the rapid conduction of electrical signal.

The excitability of cardiac myocytes is facilitated by ionic currents through different ion channels located in the cell membrane of the cardiac myocytes. The main ion channels involved in the generation of action potentials are sodium channels, potassium channels and calcium channels. A typical action potential generated by a ventricular myocyte consists of 5 phases. During phase 0 of the action potential, fast depolarization of the cardiac myocyte occurs as sodium channels open to allow sodium current to flow from the extracellular space into the cytoplasm. Phase 1 of the action potential involves inactivation of sodium channels and activation of I_{kto}, which allows early repolarization of the cells and gives the 'notch' in action potential morphology. During phase 2, both L-type calcium channels and delayed rectifier potassium channels are activated and the two currents balance out so that the action potential reaches a plateau. In phase 3, which is the repolarization phase, calcium channels are inactivated and potassium current dominates to allow repolarization of cardiac myocytes back to their resting phase. At the resting phase, I_{k1}, the inward rectifier, is dominant. A myocyte is only excitable when it is non-refractory, i.e. when excitable channels have fully recovered, which corresponds to late repolarization or resting phase. Action potential duration (APD) depends on the duration

of the diastolic interval; diastolic interval is the difference between the coupling interval between the two stimuli and the APD. The relationship between APD versus diastolic interval is termed APD restitution relation, which is an important determinant of scroll wave stability (see 1.1.2 Cardiac arrhythmias for definition of scroll waves); a maximal APD restitution slope of >1 has been shown to promote scroll wave breakup (1).

Cardiac myocytes exhibit different action potential morphologies transmurally. Action potential in epicardial cells (cells in the outermost layer of the myocardium) has a more prominent 'spike and dome' morphology compared to that in the endocardium (innermost layer of the myocardium) and mid-myocardium (middle layer of the myocardium). Action potential in the mid-myocardium is longer than that in the epicardium and endocardium. The different action potential morphologies of various cell types coordinate the electrical and mechanical activity of the myocardium and thus allow proper function of the heart.

1.1.2 Cardiac arrhythmias

Cardiac arrhythmias are any disturbances of normal cardiac rhythm. Abnormally slow rhythms (<60 bpm) are called bradyarrhythmias and abnormally fast rhythms (>100 bpm) are called tachyarrhythmias. The most severe type of arrhythmias is fibrillation, which is completely disorganized electrical state that mostly degenerates from tachycardia.

One important mechanism for tachyarrhythmias is reentry. Reentry is characterized by an abnormal activation wavefront which reenters a previously-excited region and forms a circular electrical loop. Three conditions have to be met for reentry to occur: 1) an excitation wave has to encounter conduction block; 2) propagation of the excitation

wave along an alternate pathway around area of block is allowed (unidirectional block); 3) the propagation wave must always find excitable tissue in the direction of propagation. The last requirement implies that the reentry circuit pathway has to be longer than the wavelength, which is given by the product of conduction velocity (CV) and effective refractory period (a period of time following an action potential during which a new action potential cannot be initiated).

Reentry can be either anatomical or functional. In anatomical reentry, a central physical (non-conducting) obstacle such as scar tissue that forces the wave to take a detour around it has to be present. In functional reentry, no physical obstacle is required as it is created by refractory tissue. Scroll waves are formed in functional reentry and the core of reentry is unexcited excitable tissue.

The re-entrant wave in tachycardia exhibits a relatively stable and repeatable pattern. However, tachycardia also degenerates into fibrillation when the activation wavefront breaks up into multiple re-entrant circuits and no longer repeats its stable cycle of activation. In ventricular fibrillation (VF), activation occurs chaotically throughout the ventricular tissue which results in uncoordinated contraction of myocardium, failed pumping of blood into the circulatory system and thus sudden cardiac death within minutes. Tachycardia and fibrillation can be differentiated on the electrocardiogram (ECG): fast and regular ECG is a manifestation of tachycardia, whereas irregular and complex ECG demonstrates the existence of fibrillation.

Scroll wave filaments are the organizing centers of scroll waves. The number of filaments throughout the ventricular tissue can be used to assess the stability of scroll waves. The larger the number of scroll wave filaments, the more unstable the scroll

waves. There are usually very few filaments in tachycardia, but there are multiple filaments in fibrillation.

1.1.3 Excitation-contraction coupling and sliding filament mechanism

The cell membrane has deep invaginations called T-tubules in which most of the L-type calcium channels are located. During the plateau phase of the action potential, L-type calcium current flows into the cytoplasm, triggering release of large amount of calcium from sarcoplasmic reticulum (SR) into cytoplasm through ryanodine receptor. Calcium-induced calcium release is graded with the amount of trigger calcium and the amount of calcium in SR. Calcium then activates myofilaments and allows contraction of the myocardium.

Contraction of cardiac myocytes is a result of cyclical interactions between the contractile proteins actin and myosin. Actin and myosin are arranged in a regular lattice of units called sarcomere. Actin is a thin filament that is arranged as a two-stranded helix of actin monomers. Myosin is a thick filament with myosin heads attached. After calcium-induced calcium release, calcium first binds to troponin C. Cooperative conformational changes then occur in the troponin-tropomyosin system to expose actin sites and thus inhibition of actin and myosin interaction is released. The crossbridges of myosin heads on the thick filaments then attach to actin filaments. Consequently, tension is exerted and the muscle shortens.

To allow relaxation of the myocardium, calcium is removed mostly through the SR Ca^{2+} ATPase pump into SR. Some of the calcium is removed through sodium-calcium exchanger and sarcolemmal Ca-pump. Calcium comes off troponin C as a result of the

deficiency of calcium in the fluid around the myofibrils. Troponin-tropomyosin inhibits interaction of actin and myosin. As a result, crossbridges are detached from the thin filaments. Active tension decreases back to resting value and the rest length is restored.

1.2 Mechano-electric feedback (MEF)

MEF is the modulation of cardiac electrical activity by cardiac mechanics. Mechanical stimulation has long been found to cause electrical activity in the heart (2). However, the molecular mechanisms through which mechanical stimulation induces electrical activity are still unclear. It has been suggested that stretch-activated channels (SACs) are involved in mechanically induced electrical activities. SACs are ion-conducting channels in the cell membrane that open in response to positive strain (3, 4). Many single-channel and whole-cell studies on cardiomyocytes have been conducted and the presence of SACs in a wide variety of cardiomyocytes has been proved (5). Many different types of ion channels have been identified including the non-selective cation SAC and potassium conducting SAC. The reversal potential for a non-selective cation SAC has been reported to be halfway between the resting membrane potential and the action potential plateau (5-8). Recruitment of non-selective cation SACs results in depolarization, possibly ectopic beats during diastole; recruitment of non-selective cation SAC during systole speeds up early repolarization and prolongs late repolarization, resulting in a crossover of action potentials and prolongation of APD. The reversal potential of a potassium-conducting SAC has been reported to be more negative than the

resting membrane potential (9-11). Recruitment of potassium-conducting SACs causes repolarization during systole and results in shortening of APD.

1.3 Cardiac resynchronization therapy

Heart failure is a major cause of morbidity and mortality (12), contributing significantly to global health expenditure. A large number of heart failure patients exhibit a left bundle branch block (LBBB) type of electrical activation. In such patients, the LV is activated through the septum from the RV, resulting in a delayed onset of LV contraction relative to that of the RV (13). Cardiac resynchronization therapy (CRT), which employs bi-ventricular pacing to re-coordinate the contraction of the heart, has been demonstrated to be a valuable therapeutic option for such patients (14). CRT typically involves implantation of three leads, one into RA, and two in the RV and LV, respectively. The two ventricular electrodes provide stimuli simultaneously to elicit a synchronous contraction. The pacing time interval between activating the RA and the subsequent activation of both ventricles (atrioventricular, AV, delay) is often optimized to additionally improve the acute hemodynamic response of the heart.

1.4 Motivation

The motivation for this research was to fill gaps in the current understanding of the electromechanical interactions in the heart, with the expectation that this improved understanding will lead to better treatment for cardiac diseases, specifically cardiac arrhythmias and dyssynchronous heart failure (DHF). In this study, the effects of MEF on

scroll wave stability in human VF were examined. The mechanisms underlying the acute response of CRT, specifically stroke work improvement, were explored. Lastly, the feasibility of optimizing CRT pacing locations to both improve the hemodynamics and result in ATP consumption homogeneity throughout the LV was demonstrated. The motivation for these choices is given below.

1.4.1 Effects of MEF (recruitment of SAC) on scroll wave stability

Opening of SAC has been demonstrated to depolarize the resting membrane and thus cause Na channel inactivation (6, 15), which can stabilize scroll waves (16), the waves that underlie reentrant arrhythmias. On the other hand, SAC-induced depolarization and Na channel inactivation have been shown to give rise to scroll wave breakup (17) that increases electrical instability and leads to turbulent behavior underling the most lethal arrhythmias. These contradictory results indicate that the conditions under which and the mechanisms by which recruitment of SAC alters scroll wave stability remain incompletely understood.

1.4.2 Predominant mechanism underlying stroke work improvement in the acute response of CRT

The acute response of the DHF ventricles to CRT is believed to be due to 3 main mechanisms: resynchronization of ventricular contraction, efficient preloading of the ventricles by a properly timed atrial contraction, and reduced mitral regurgitation (18). The acute response to CRT is manifested by an augmentation in stroke work (19). However, the contribution of each of the three mechanisms to stroke work improvement

during the acute response to CRT has not been quantified and therefore, the predominant mechanism underlying this improvement has not been identified.

1.4.3 Optimizing CRT to minimize ATP consumption heterogeneity throughout the LV

CRT has been demonstrated to lead to the restoration of oxygen consumption homogeneity throughout the LV, which is important for long-term reverse remodeling of the ventricles. However, research has focused exclusively on identifying the LV pacing sites that led to acute hemodynamic improvements. It remains unclear whether there exist LV pacing sites that could both improve the hemodynamics and result in ATP consumption homogeneity throughout the LV, thus maximizing both CRT short-term and long-term benefits.

1.5 Aims

It was the goal of this study to improve the understanding of the electromechanical interactions in the heart and to explore ways to improve therapies for cardiac diseases such as cardiac arrhythmias and DHF.

The three aims for this project were:

Specific Aim 1: Develop a strongly-coupled model of human ventricular electromechanics that incorporated human ventricular geometry and fiber and sheet orientation reconstructed from MR and diffusion tensor (DT) MR images, and determine the effects of recruitment of SAC with different reversal potential and

channel conductance on scroll wave stability and uncover the relevant mechanisms underlying the different behaviors.

Specific Aim 2: Using an magnetic resonance image (MRI)-based anatomically accurate 3D model of failing canine ventricular electromechanics, quantify the contribution of each of the three mechanisms to stroke work improvement and identify the predominant mechanisms.

Specific Aim 3: Using an MRI-based anatomically accurate 3D model of failing canine ventricular electromechanics, demonstrate the feasibility of optimizing CRT pacing locations to achieve maximal improvement in both ATPCTHI (an ATP consumption heterogeneity index) and stroke work.

Chapter 2

Overarching Methods

Efforts to investigate the electromechanical interactions in the heart are hampered by the lack of experimental methodology that can record the 3D electrical and mechanical activity simultaneously with high spatiotemporal resolution. Thus, 3D modeling of cardiac electromechanics serves as an attractive alternative for analyzing the electromechanical interactions in the heart. This chapter presents both the electrical model and the mechanical model used in this study with more emphasis on the finite element principles used in the mechanical model.

2.1 Electromechanical model

To represent cardiac tissue in 3D, finite element models were used. The image-based 3D electromechanical model of the human ventricles (chapter 3) incorporates realistic ventricular geometry and fiber-sheet architecture reconstructed from high-resolution MR and DTMR images (20). The model consists of an electrical and a mechanical component, which are coupled via the intracellular calcium dynamics (21, 22). The ventricular geometry and fiber-sheet architecture of the failing canine model (chapter 4 and 5) were constructed from high-resolution MR and DTMR images of DHF canine ventricles. For computational tractability, the electrical and mechanical components of the electromechanical model of the DHF canine ventricles were weakly coupled.

2.2 Modeling cardiac electrophysiology and excitation-contraction coupling

The first quantitative model of an electrically excitable cell was developed by Hodgkin and Huxley (HH) (23). The cell membrane is modeled as a capacitor. The different types of ion channels are modeled as resistors, each with its own unique current-voltage relationship to reflect the selective permeability of each ionic species. The HH model forms the basis for all the cardiac myocyte models developed in the following decades.

Cardiac myocyte models have advanced tremendously since the HH model. The more recent models include many more types of ionic channels and thus are able to reproduce many more properties of cardiac myocytes. The ionic models used in the studies include the ten Tusscher et al. ionic model of the human ventricular myocyte (24) and the Luo-Rudy dynamic model (25). Ca transient from the ionic model (chapter 3) was fed into the Rice et al. myofilament model (26), which was used to represent active tension generation.

Monodomain equations were used to describe cardiac electricity, as the extracellular field contribution in the studies could be ignored. Intra- and extracellular spaces were modeled together as 'bulk' tissue, which yields computational savings. The cardiac tissue was assumed to be orthotropic, meaning the electrical properties of the cardiac tissue were different in different directions.

2.3 Modeling cardiac mechanics

2.3.1 Governing equations

The governing equation was based on conservation of linear momentum following Newton's laws of motion. For static equilibrium in the absence of body forces, the strong form of the governing equation was given by

$$\frac{\partial}{\partial X_M}\left(T^{MN}F_N^j\right) = 0 \quad \text{(2.1)}$$

where X=$\{X_m\}$ were the coordinates of a material point in the undeformed coordinate system and F_N^j were the components of the deformation gradient tensor given by

$$F_N^j = \frac{\partial x_j}{\partial X_N} \quad \text{(2.2)}$$

where x =$\{x_j\}$ were the coordinates of a material point in the deformed coordinate system. T_{MN} were the components of the second Piola-Kirchhoff tensor, which represented force per unit undeformed area acting on an infinitesimal element of surface in the reference configuration. This tensor could be calculated as derivatives of strain energy density function W

$$T_{MN} = \frac{1}{2}\left(\frac{\partial W}{\partial E_{MN}} + \frac{\partial W}{\partial E_{NM}}\right) \quad \text{(2.3)}$$

where E_{MN} were the components of Lagrangian Green's strain tensor given by

$$E = \frac{1}{2}(C - I) \quad \text{(2.4)}$$

where I was the identity matrix and C was the Cauchy-Green deformation tensor given by $F^T F$

The strain energy density function W served as the constitutive law which expressed the experimentally observed relationship between a material's stress and strain tensors.

Certain material properties could impose restrictions on the form of W. For isotropic materials which exhibited identical material properties in all directions, W could be expressed in the form

$W = b_1(I_1 - 3) + b_2(I_2 - 3)$……...(2.5)

where b_1 and b_2 were the material constants with units of stress (kPa); I_1 was the trace of C (trC) and I_2 was $\frac{1}{2}[(trC)^2 - trC^2]$.

In this study, cardiac tissue was modeled as an orthotropic, hyperelastic nearly-incompressible material (21, 27, 28) whose passive properties were defined by an exponential strain energy function. Thus W is expressed in the form

$w = \frac{1}{2}w_c(e^Q - 1)$……..……...……...…..…..…..(2.6)

$Q = b_{ff}E_{ff}^2 + b_{ss}E_{ss}^2 + b_{nn}E_{nn}^2 + b_{fs}(E_{fs}^2 + E_{sf}^2) + b_{fn}\left(E_{fn}^2 + E_{nf}^2\right) + b_{ns}(E_{ns}^2 + E_{sn}^2)$……...……(2.7)

where E_{ij} referred to the local fiber coordinate system consisting of fiber (f), sheet (s) and sheet-normal (n) coordinate directions. b_{ff}, b_{ss}, b_{nn}, b_{fs}, b_{fn} and b_{ns} were the material constants that scaled the material stiffness in different directions.

2.3.2 Finite element interpolation

The undeformed and the deformed coordinates were approximated using tricubic hermite finite element interpolation

$X_M = \Psi_n(\{\xi_k\})X_M^n$……..……..….(2.8)

$x_i = \Psi_n(\{\xi_k\})X_i^n$……..……..……...(2.9)

where $\Psi_n(\{\xi_k\})$ were the interpolation function and X_M^N and x_i^N were the undeformed and deformed coordinates defined at finite element nodes (n).

Virtual displacement field {v} could be approximated using the same interpolation function

$$\delta v_j = \Psi_n(\{\xi_k\})\delta v_j^n \quad \text{.....(2.10)}$$

where δv_j^n were virtual nodal displacements and could be substituted into the weak form of the stress equilibrium equation

$$\int_{V_0} T^{MN} F_N^j \frac{\partial(\delta v_j)}{\partial X_M} dV_0 = \int_{S_2} s \cdot \delta v dS \quad \text{.....(2.11)}$$

where V_0 was the undeformed volume and S_2 was the portion of the boundary subject to external tractions (pressures), s. Both the strong form presented in the previous section and the weak form of the stress equilibrium equations could be derived via the principle of virtual work. After substituting virtual displacement, the weak form of stress equilibrium became

$$\int_{V_0} T^{MN} F_N^j \frac{\partial \Psi_n}{\partial X_M} dV_0 = \int_{S_2} p \cdot \Psi_n n_j dS \quad \text{.....(2.12)}$$

where p was the external force or pressure that acted in the normal direction to the surface and $\{n_j\}$ was the normal to the surface. After substituting the variables, the equation became

$$\iiint_0^1 T^{MN} F_N^j \frac{\partial \Psi_n}{\partial X_M} |J| d\xi_1 d\xi_2 d\xi_3 = \int_{S_2} p \cdot \Psi_n n_j dS \quad \text{.....(2.13)}$$

where the Jacobian of the coordinate transformation was defined by

$$J = \left| \frac{\partial \xi_p}{\partial X_Q} \right| \quad \text{.....(2.14)}$$

For the nodes that did not belong to a surface which had a pressure applied to i.e. there was no external nodal traction force

$$\iiint_0^1 T^{MN} F_N^j \frac{\partial \Psi_n}{\partial X_M} |J| d\xi_1 d\xi_2 d\xi_3 = 0 \quad \text{.....(2.15)}$$

For the nodes that belonged to surfaces which had pressure applied

$$\iiint_0^1 T^{MN} F_N^j \frac{\partial \Psi_n}{\partial X_M} |J| d\xi_1 d\xi_2 d\xi_3 = \int_{S_2} p \cdot \Psi_{\mathrm{n}} r d\xi_1 d\xi_2 \quad \text{.....(2.16)}$$

Since Ψ_{n} was a function of local finite element coordinates i.e. $d\Psi_{\mathrm{n}} = \begin{pmatrix} \frac{\partial \Psi_{\mathrm{n}}}{\partial \xi_1} \\ \frac{\partial \Psi_{\mathrm{n}}}{\partial \xi_2} \\ \frac{\partial \Psi_{\mathrm{n}}}{\partial \xi_3} \end{pmatrix}$

Using chain rule, we could express

$$\frac{\partial \Psi_{\mathrm{n}}}{\partial \xi_{\mathrm{i}}} = \sum_{\mathrm{k}} \frac{\partial \Psi_{\mathrm{n}}}{\partial \mathrm{X_k}} \frac{\partial \mathrm{X_k}}{\partial \xi_{\mathrm{i}}} \Longrightarrow \mathrm{J}^{\mathrm{T}} \begin{pmatrix} \frac{\partial \Psi_{\mathrm{n}}}{\partial \mathrm{X}_1} \\ \frac{\partial \Psi_{\mathrm{n}}}{\partial \mathrm{X}_2} \\ \frac{\partial \Psi_{\mathrm{n}}}{\partial \mathrm{X}_3} \end{pmatrix} = \begin{pmatrix} \frac{\partial \Psi_{\mathrm{n}}}{\partial \xi_1} \\ \frac{\partial \Psi_{\mathrm{n}}}{\partial \xi_2} \\ \frac{\partial \Psi_{\mathrm{n}}}{\partial \xi_3} \end{pmatrix} \quad \text{.....(2.17)}$$

The integrals could be expressed as

$$\iiint_0^1 T^{MN} F_N^j (J^{-1})^T d\Psi_{\mathrm{n}} |J| d\xi_1 d\xi_2 d\xi_3 = \int_{S_2} p \cdot \Psi_{\mathrm{n}} r d\xi_1 d\xi_2 \quad \text{.....(2.18)}$$

The integrals were evaluated using four point Gaussian quadrature in each of the three local finite element directions.

2.3.3 Boundary conditions and numerical solver

Boundary conditions were applied to simulate physiologically realistic constraints. For example, the nodal coordinates and their circumferential and transmural derivatives

were constrained at the base to approximate the effects of the relatively stiff annuli of the valves.

The program was parallelized and run on a cluster of approximately 100 processors.

Chapter 3

Effects of mechano-electric feedback on Scroll Wave Stability in Human Ventricular Fibrillation[1]

3.1 Introduction

Experimental and clinical research has demonstrated that the mechanical environment of the heart, in health and disease, is capable of exerting influence on cardiac electrophysiology (29). Temporal changes in strain take place during all phases of the cardiac cycle. Abnormal electrical propagation during arrhythmias also leads to abnormal strain distributions in the heart, which in turn could affect electrical propagation. The mechanisms that contribute to strain-dependent modulation of electrical wave propagation are termed MEF mechanisms (30).

There are several MEF mechanisms in the heart, including stretch-induced changes in intracellular Ca handling (31), depolarization of cardiac fibroblasts by stretch (via mechano-sensitive ion channels) affecting the resting potential and APD of the coupled myocyte (32), and most importantly, myocyte sarcolemmal channel activation by mechanical stimuli (5, 33). SAC, a type of mechanically activated ionic channels identified in cardiac tissue, have been found responsible for the generation of arrhythmias

[1]This chapter was published in ref. 27. Hu Y, Gurev V, Constantino J, Bayer JD, Trayanova NA. Effects of mechano-electric feedback on scroll wave stability in human ventricular fibrillation. PloS one. 2013;8(4):e60287. Epub 2013/04/11.

Contributions other than the author's: Dr. Viatcheslav Gurev and Dr. Jason Constantino co-developed the model with the author. Dr. Jason Bayer was responsible for part of the data analysis.

following an appropriately timed mechanical impact to the heart (commotio cordis) (34, 35), as well for the termination of ventricular arrhythmias following a precordial thump (36). Abnormal deformation associated with the establishment of arrhythmia can also affect the progression of the arrhythmia itself; this aspect of MEF has received less attention in the literature.

On one hand, opening of SAC has been demonstrated to depolarize the resting membrane and thus cause Na channel inactivation (6, 15), which can stabilize scroll waves (16), the waves that underlie reentrant arrhythmias. On the other hand, SAC-induced depolarization and Na channel inactivation have been shown to give rise to scroll wave breakup (17) that increases electrical instability and leads to turbulent behavior underling the most lethal arrhythmias. These contradictory results indicate that the conditions under which and the mechanisms by which recruitment of SAC alters scroll wave stability remain incompletely understood.

To provide a comprehensive understanding of the mechanisms by which SAC opening affects the stability of scroll waves, it is necessary to record, in 3D, both the electrical and mechanical activity simultaneously, and at a high spatiotemporal resolution. Currently, this is not possible by means of experimentation. In contrast, biophysically-detailed computer simulations of electromechanical function at the organ scale have the capability to dissect the relationship between stretch and arrhythmia maintenance; initial attempts in this direction have already been made (37, 38). The latter simulation studies had focused predominantly on the effect of recruitment of SACs with large conductances and reversal potentials close to zero on scroll wave stability. However, SACs have been demonstrated to exhibit a wide variety of reversal potentials and

conductances (5). Opening of SAC with a reversal potential close to the resting membrane potential has been shown to shorten APD (9), while opening of SAC with a less negative reversal potential has been found to have the opposite effect, resulting in APD prolongation (39). The degree of lengthening or shortening of APD is affected by SAC conductance as well. Since recruitment of SAC with different reversal potentials and conductances leads to different electrophysiological changes in cardiac myocytes, it is thus possible that SAC opening could affect scroll wave stability in the 3D heart via different mechanisms depending on the channel population characteristics.

The goal of this study was to conduct a comprehensive analysis of the effects of SAC recruitment on scroll wave stability in the fibrillating ventricles. To achieve this goal, a strongly-coupled MRI-based biophysically-detailed electromechanics model of the human ventricles was developed. We used this model (1) to test the hypothesis that recruitment of SAC affects scroll wave stability differently depending on the reversal potential and channel conductance of SAC and (2) to uncover the relevant mechanisms underlying the different behaviors.

3.2 Materials and Methods

3.2.1 Electromechanical model

The image-based 3D electromechanical model of the human ventricles developed for this study as shown in Figure 3.1A incorporates realistic ventricular geometry and fiber-sheet architecture reconstructed from high-resolution MR and DTMR images (20). The model consists of an electrical and a mechanical component (Figure 3.1B), which are coupled via the intracellular calcium dynamics (21, 22).

Mathematical description of the electrical component of the model was based on the monodomain representation of cardiac tissue; our group has made extensive use of such large-scale electrophysiological models of the heart (40). Membrane kinetics were represented by the ten Tusscher et al. ionic model of the human ventricular myocyte (24). To make the substrate prone to arrhythmia, the maximum conductances of the IKr, IKs, IpCa, and IpK currents and the time constant for the f gate of the L-type calcium current were modified throughout the ventricles, as described in (41), producing a steep local APD restitution curve with a maximum slope of 1.8.

The mechanical component incorporated a continuum mechanics model of the ventricles and a lumped-parameter model of the circulatory system, both of which have been described previously (21). The parameters in the circulatory system model were adjusted for the human ventricles using available physiological data (42); parameter values are presented in the Table 3.1. Active tension generation in the mechanics component was represented by the Rice et al. model of myofilament dynamics (26). To simulate reduced contractility during arrhythmias, the half-activation constant for shift of a regulatory unit to a permissive state in the Rice et al. model was increased by 20% to decrease the sensitivity of troponin to Ca; this ensured that the maximal pressure during VF matched that observed clinically (43).

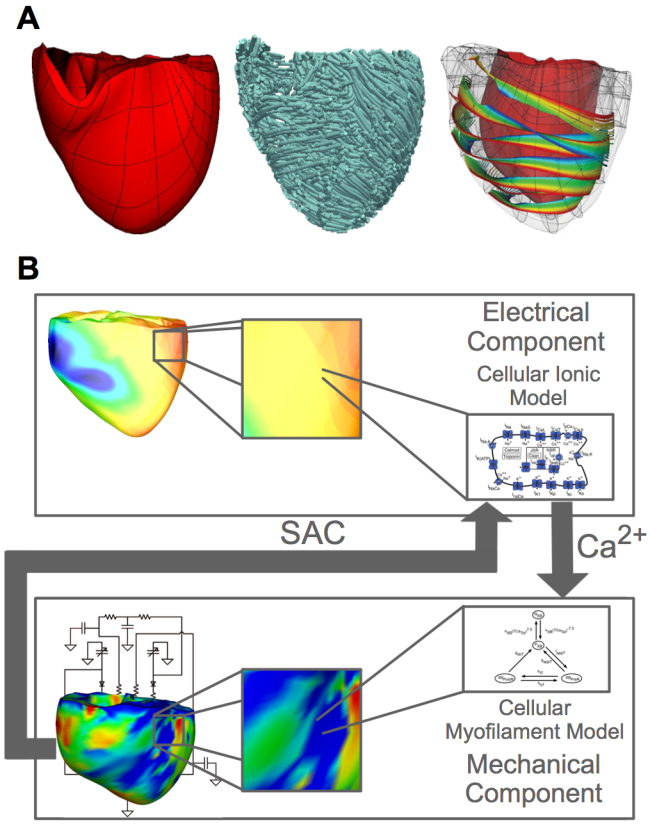

Figure 3.1: MRI-based electromechanical model of the human ventricles. **(A):** The mechanical mesh, fiber orientation and sheet structure of the human ventricular model. **(B):** The schematic diagram of the electromechanical model.

The electrical mesh consisted of 4274379 elements with a spatial resolution of 500μm; our electrical meshes are always tested for convergence (for the specific solvers we used; descriptions can be found in (44)). Description of the electrical mesh generation procedure can be found in Prassl et al. (45) The mechanical mesh (21) was a nonlinear mesh with 230 hexahedral elements. The spatial resolution for the mechanical mesh was 10mm. The methodology for the generation of the mechanical mesh is described in Gurev et al (21).

Table 3.1: Adjusted parameters of the Kerckhoffs et al. circulatory model.

Time-varying elastance atrial model		**Systemic circulation**		**Pulmonic circulation**	
$E_{LA,max}$	0.0782 kPa/ml	R_{mitral}	$1*10^{-4}$ kPa*s/ml	R_{tricus}	$1*10^{-4}$ kPa*s/ml
$E_{LA,min}$	0.0711 kPa/ml	R_{ao}	0.007 kPa*s/ml	R_{pa}	0.004 kPa*s/ml
$V_{LA,rd}$	64.6 ml	R_{as}	0.124 kPa*s/ml	R_{ap}	0.011 kPa*s/ml
$V_{LA,rs}$	60 ml	R_{vs}	0.02 kPa*s/ml	R_{vp}	0.011 kPa*s/ml
$E_{RA,max}$	0.03 kPa/ml	C_{as}	97.8 ml/kPa	C_{ap}	125.1 ml/kPa
$E_{RA,min}$	0.0273 kPa/ml	C_{vs}	1299 ml/kPa	C_{vp}	150.0 ml/kPa
$V_{RA,rd}$	64.6 ml				
$V_{RA,rs}$	60 ml				

The electrical and mechanical components of the model were strongly coupled. A mechanical solution step (500μs) followed every five electrical solution steps (100μs). During electrical propagation, the spatial distribution of intracellular Ca concentration throughout the ventricles was calculated from the ionic model at each node in the electrical component computational mesh and then, at every fifth solution step, mapped onto the Gaussian points in the mechanical computational mesh. At every Gaussian point, the local intracellular Ca concentration was inputted into the myofilament model to generate the local active tension. After solving for the mechanical deformation of the ventricles arising from the active tension, strain tensors were mapped back onto the nodes

in the electrical computational mesh. From the strain tensor at each node, the local stretch ratio in the fiber direction was determined and used to calculate the local SAC current (see below for formulation) at that node, which in turn affected global propagation. The electromechanical model detailed above has been extensively validated by our group using electromechanical wave imaging (46). Numerical approaches to solving the equations of the electromechanical model used methodologies described elsewhere (21, 47). This state-of-the-art human electromechanical model is of broad applicability and can be used in a wide range of studies in cardiac electromechanics.

3.2.2 MEF

Consistent with the goal of the study, SACs were incorporated in the electromechanical model of the human ventricles; opening of SAC was the mechanism by which mechanical deformation provided feedback into the electrical activity of the heart. The possible effect of mechanical deformation on geometry was not incorporated into the model to decrease model complexity and because it has been demonstrated to not affect scroll wave stability (38). Since the current through SAC, I_{SAC}, has been shown to increase linearly with stretch (39), I_{SAC} was formulated as being linearly proportional to the stretch ratio in the fiber direction, λ_f:

$I_{SAC} = g_{SAC}(\lambda_f - 1)(V_m - V_{SAC})$ if $\lambda_f > 1$; $I_{SAC} = 0$ if $\lambda_f \leq 1$……..……(3.1)

where V_m is the transmembrane potential, and V_{SAC} is the reversal potential of SAC. SACs were assumed to conduct only when λ_f was larger than 1 (48); thus, I_{SAC} was zero during myofiber shortening. Since I_{SAC} is the total current through both non-selective cation and potassium-conducting SACs, the value of V_{SAC} depends on the degree of the

relative expressions of non-selective cation and potassium-conducting channels in myocardial tissue. Given that non-selective cation SACs have been reported to have a reversal potential of 0mV (7) and potassium-conducting SACs operate with a reversal potential of -90mV (11), V_{SAC} can range between -90mV and 0mV. In this study, we used two values of V_{SAC} that spanned that range, one close to the membrane resting potential (-60mV (49)) and another less negative (-10mV (39)). The SAC conductance g_{SAC} was varied between 0 and 0.07mS/μF (29, 50, 51) to fully investigate the effects of SAC recruitment on scroll wave stability.

3.2.3 VF induction protocol

To induce VF, the ventricles were first paced seven times from the apex at a 700ms basic cycle length to achieve steady-state propagation. Then, at 500ms following the last pacing beat, a cross-field stimulation was applied to the posterior side of the ventricles, inducing reentry. Reentrant waves broke up due to the restitution properties of the myocardium, leading to VF. Simulations were run for 5 seconds post-VF induction to ensure that VF was sustained.

3.2.4 Scroll-wave Filaments and Pseudo ECGs

To analyze the stability of the scroll waves, the number of scroll-wave filaments (the organizing centers of reentry) throughout the ventricular volume was determined at time instants 200ms apart during 4 seconds of simulation using an algorithm based on phase angle maps, as described previously (52).

Pseudo ECGs were computed as follows (53):

$$ECG = \int_V \frac{D\nabla V_m \cdot \vec{r}}{r^3} dV \quad \text{.....} \quad (3.2)$$

where V is the ventricular volume, $\bar{r}$ is the vector from each point in the ventricular volume to the recording electrode, the latter placed 10cm from the center of the anterior wall of the ventricles in the anterior direction of the transverse plane, as done previously (37), and r is the distance from each point in the ventricular volume to the recording electrode.

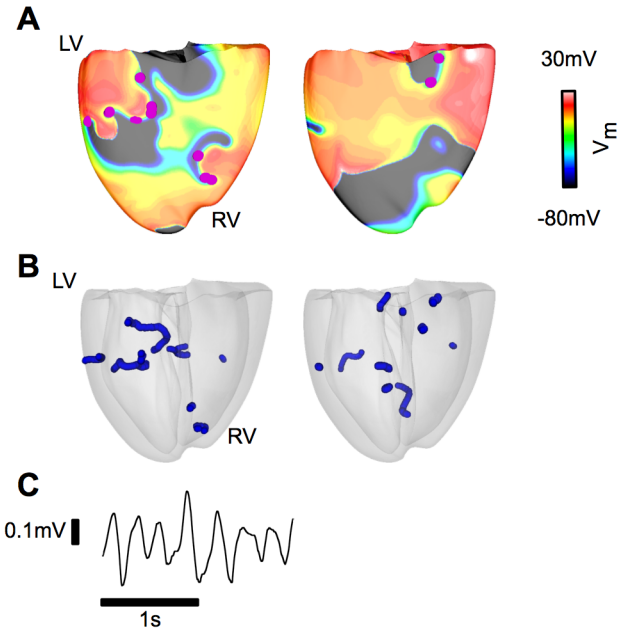

Figure 3.2: VF in the electromechanical model without SAC representation. **(A):** Epicardial transmembrane potential distribution maps on the posterior wall from the simulation without SAC representation. Pink dots indicate the locations of the phase singularities. **(B):** Posterior semi-transparent view of the ventricles shows the filament distribution (blue). **(C):** Pseudo-ECG.

3.3 Results

3.3.1 VF in the electromechanical model without SAC representation

Figure 3.2 presents the epicardial transmembrane potential distribution maps of sustained VF (Figure 3.2A) in the model without SAC representation; scroll waves break up continuously, maintaining VF. There are multiple scroll wave filaments present in the ventricles during the simulation (Figure 3.2B). The irregular and complex pseudo-ECG (Figure 3.2C) is a manifestation of the numerous meandering reentrant waves sustaining VF.

Table 3.2: The average number of filaments in the VF human ventricular electromechanical model with SAC of V_{SAC} of -60mV for different g_{SAC}.

	Average No. of filaments
Without SAC	7.6±2.2
g_{SAC} (mS/μF)	
0.03	2.9±1.0*
0.05	3.1±1.7*
0.07	4.1±1.7*

The symbol * indicates that the average number of filaments is significantly smaller than that in the model without SAC representation ($p<0.05$).

3.3.2 Inclusion of SAC with V_{SAC} of -60mV results in partial suppression of scroll wave breakup by flattening of the APD restitution curve

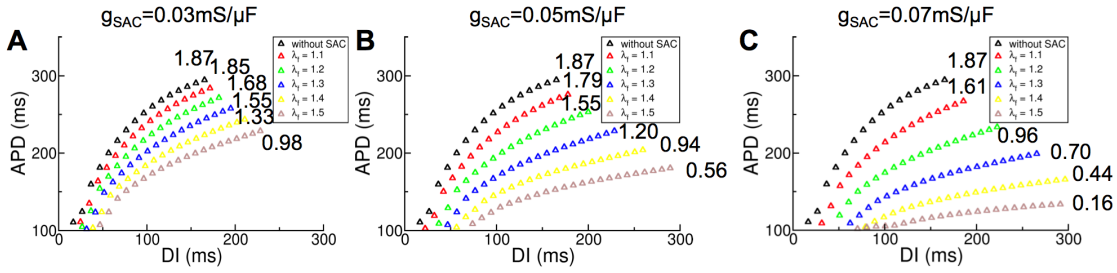

Figure 3.3: Recruitment of SAC with V_{SAC} of -60mV flattens the single-cell APD restitution curve. Changes in the single-cell APD restitution curves due to SAC opening for different values of λ_f. **(A):** g_{SAC}=0.03mS/μF, **(B):** g_{SAC}=0.05mS/μF and **(C):** g_{SAC}=0.07mS/μF.

Comparing the number of filaments in the model with and without SAC (V_{SAC} of -60mV**)** revealed that SAC activation partially suppressed (but did not eliminate) scroll wave breakup for all values of g_{SAC}. Indeed, for the model with SAC, the average number of filaments decreased by 46-62%, depending on the value of g_{SAC}, as compared to the model without SAC (Table 3.2).

To understand the mechanisms by which recruitment of SAC with V_{SAC} of -60mV decreased the likelihood of scroll wave breakup, we first investigated an important determinant of dynamic instability, the single cell APD restitution relation and its modification by MEF. Single cell APD restitution relations with SAC recruitment were calculated for the three values of g_{SAC} examined; results are presented in Figure 3.3. The strain map of the fibrillating human heart at each time instant during the simulation was analyzed (a representative strain map is shown in Figure 3.4A) and the maximum λ_f was found to be 1.5. Single-cell APD restitution curves were thus constructed for different degrees of SAC opening corresponding to λ_f values from 1.0 to 1.5. As shown in Figure

3.3, current through SAC leads to flattening of the single-cell APD restitution curve for all values of λ_f and g_{SAC}. The larger the value of λ_f or g_{SAC}, the flatter the resulting APD restitution curve.

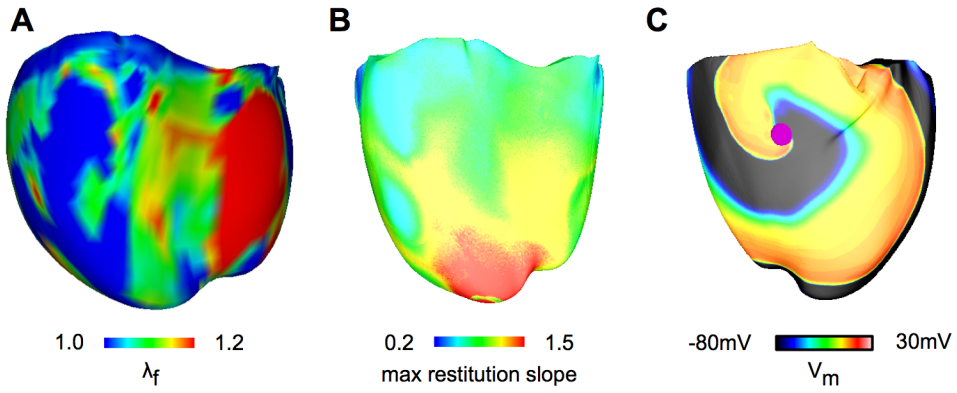

Figure 3.4: Recruitment of SAC with V_{SAC} of -60mV diminishes scroll wave breakup. **(A):** Snapshot of the heterogeneous λ_f distribution at 2.3s after arrhythmia induction for the ventricular model with V_{SAC} of -60mV; g_{SAC}=0.07mS/μF. In plotting the λ_f distribution, the range 1.0 to 1.2 was chosen for visual purposes, as 90% of the data points fell within this range. **(B):** Maximum APD restitution slope distribution for the same model and time instant as in (A). In plotting of maximum APD restitution slopes, the range 0.2 to 1.5 was chosen for visual purposes, as 97% of the data points fell within this range. **(C):** Epicardial transmembrane potential distribution map on the anterior wall for V_{SAC} of -60mV and g_{SAC} of 0.07mS/μF when λ_f was assumed constant and equal to 1.2. Pink dot indicates the location of the phase singularity.

At any time instant during VF, the distribution of λ_f in the ventricles was heterogeneous, as illustrated by the snapshot map in Figure 3.4A. This led to non-uniform I_{SAC} throughout the ventricles, which in turn gave rise to varying degrees of APD

restitution flattening in the ventricular model with SAC. A map of the distribution of maximum restitution slope in the ventricles for g_{SAC} of 0.07 mS/μF is presented in Figure 3.4B. Regions of large λ_f had maximum restitution slopes smaller than 1, whereas regions of small λ_f had maximum restitution slopes larger than 1 but less than the original value of 1.8. These regional differences in the restitution-flattening effect of SAC opening are the reason why scroll waves continued to break up (albeit much less frequently). Should λ_f have been homogeneous and of value 1.2 or above, recruitment of SAC with V_{SAC} of -60mV would have led to the conversion of VF into ventricular tachycardia, as our simulations found; Figure 3.4C shows a stable scroll-wave with a single filament throughout the simulation in this case (for λ_f=1.2 everywhere).

3.3.3 Recruitment of SAC with V_{SAC} of -10mV diminishes scroll wave breakup at low g_{SAC}, but not at large g_{SAC}.

Comparing the number of filaments that sustain VF in the ventricular model with and without SAC demonstrated that recruitment of SAC with V_{SAC} of -10mV had a different effect on the stability of scroll waves depending on the value of g_{SAC}. For low values of g_{SAC} (from 0.02 mS/μF to 0.04 mS/μF), the average number of filaments for the model with SAC decreased by 32-51% compared to that in the model without SAC (Table 3.3), indicating less frequent scroll wave breakup. For large values of g_{SAC} (0.05 mS/μF and above), the average number of filaments for the model with SAC was not significantly different from that in the model without SAC (Table 3.3), demonstrating that scroll wave breakup was not suppressed.

Table 3.3: The average number of filaments in the ventricular model with SAC of V_{SAC} of -10mV for different g_{SAC}.

	Average No. of filaments
Without SAC	7.6±2.2
g_{SAC} (mS/μF)	
0.01	7.3±3.1
0.02	4.4±1.6*
0.03	3.7±1.0*
0.04	5.2±2.1*
0.05	7.4±1.3
0.06	8.0±2.8
0.07	8.9±2.4

The symbol * indicates that the average number of filaments is significantly smaller than that in the model without SAC representation ($p<0.05$).

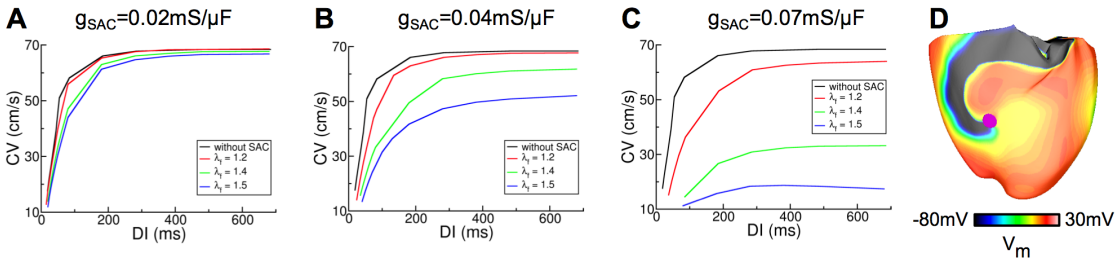

Figure 3.5: Recruitment of SAC with V_{SAC} of -10mV diminishes scroll wave breakup at low g_{SAC}. Changes in the CV restitution curves due to SAC opening for different values of λ_f. **(A):** g_{SAC}=0.02mS/μF, **(B):** g_{SAC}=0.04mS/μF and **(C):** g_{SAC}=0.07mS/μF. **(D):** Epicardial transmembrane potential distribution map on the anterior wall for V_{SAC} of -10mV and g_{SAC}=0.04mS/μF when λ_f was assumed constant and equal to 1.2. Pink dot indicates the location of the phase singularity.

To understand the mechanisms by which opening of SAC with V_{SAC} of -10mV diminishes scroll wave breakup at low g_{SAC}, we first determined the single cell APD restitution curves with SAC recruitment in this case and found that opening of SAC with V_{SAC} of -10mV does not change the single cell APD restitution curves. Since previous studies have shown that flattening of CV restitution curves also leads to stabilization of scroll waves (54, 55), we next determined the CV restitution curves with SAC recruitment for all g_{SAC} values using a model of a slab of human ventricular tissue as done previously (56). The results for three representative g_{SAC} values, 0.02, 0.04 and 0.07 mS/μF, are shown in Figure 3.5. Analysis of the ventricular strain maps for all time instants showed that in this case the maximum λ_f was also 1.5, despite the differences in the spatial distribution of strain. Thus, CV restitution curves were constructed for different degrees of SAC opening corresponding to λ_f of 1.0, 1.2, 1.4 and 1.5. As demonstrated in Figure 3.5A-C, current through SAC leads to flattening of the CV restitution curves for all values of λ_f and g_{SAC}. The larger the value of λ_f or g_{SAC}, the flatter the CV restitution curve.

Heterogeneous distribution of λ_f throughout the ventricles as demonstrated in Figure 3.4A gave rise to different degrees of SAC opening and thus CV restitution curve flattening. The flatter CV restitution curve in regions of substantial stretch resulted in suppression of scroll wave breakup there; the still-steep CV restitution curve in regions of minimal stretch continued to promote scroll wave breakup. As a result, the degree of spiral wave breakup and thus the number of filaments in the ventricles diminished. If the distribution of λ_f (of value 1.2 or above) were homogeneous, opening of SAC with V_{SAC}

of -10mV would have completely suppressed scroll wave breakup, as shown by the stable scroll waves throughout the simulation in Figure 3.5D (for λ_f=1.2 everywhere).

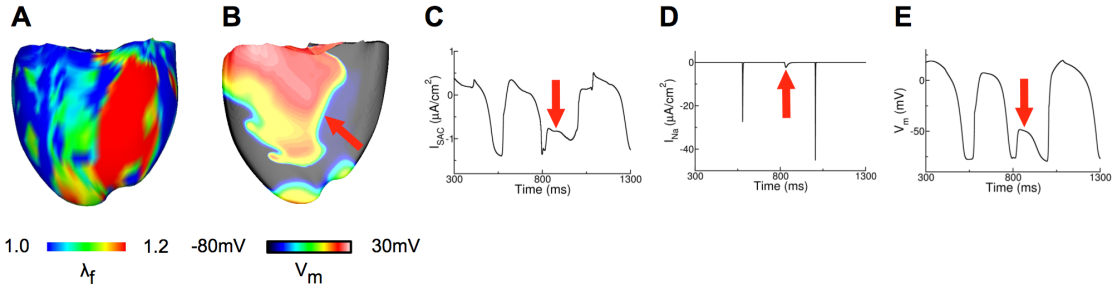

Figure 3.6: Recruitment of SAC with V_{SAC} of -10mV results in scroll wave breakup at large g_{SAC}. **(A):** Distribution of λ_f at 0.9s after arrhythmia induction for the ventricular model with V_{SAC} of -10mV; g_{SAC}=0.07mS/μF. **(B):** Scroll wave breakup in the region of large stretch (indicated by arrow). **(C), (D) and (E)** are plots of I_{SAC}, I_{Na} and V_m, respectively from the node indicated by the arrow in (B). The arrow denotes in (C): the large inward I_{SAC} during repolarization, in (D): inactivation of Na channels, (E): conduction block.

For large values of g_{SAC}, opening of SAC with V_{SAC} of -10mV in regions of substantial stretch (Figure 3.6A) resulted in a large inward I_{SAC} during repolarization (Figure 3.6C), which elevated the resting membrane potential from -85mV in the model without SAC to -77mV in the ventricles with SAC (Figure 3.6E) and thus inactivated the Na channels in the latter model (Figure 3.6D). As a result, conduction block occurred in regions of substantial stretch (Figure 3.6E) causing scroll wave breakup there (Figure 3.6B). The scroll wave breakup in regions of substantial stretch counteracted the increased scroll wave stability due to a flatter CV restitution there (Figure 3.5C),

explaining why the number of scroll wave filaments in the model with SAC was not significantly different from that in the model without SAC at large values of g_{SAC}.

3.4 Discussion

This study investigated the effects of SAC opening on scroll wave stability in the fibrillating ventricles by employing a strongly-coupled MRI-based anatomically accurate 3D model of human ventricular electromechanics. A comprehensive analysis of how recruitment of SAC influences scroll wave breakup was performed for different SAC reversal potentials and channel conductances. We discovered that recruitment of SAC affects scroll wave stability via different mechanisms depending on the reversal potential and channel conductance of SAC.

1. Opening of SAC with V_{SAC} of -60mV decreases the likelihood of scroll wave breakup for all values of g_{SAC}. The underlying mechanism is flattening of the APD restitution curve in regions of high strain.
2. Opening of SAC with V_{SAC} of -10mV partially inhibits scroll wave breakup at low values of g_{SAC} by flattening the CV restitution relation in regions of high stretch. For large values of g_{SAC}, recruitment of SAC with V_{SAC} of -10mV did not diminish the likelihood of scroll wave breakup because Na channel inactivation in regions of large stretch (as a result of SAC opening) led to conduction block and thus scroll wave breakup, which counteracted the increased scroll wave stability due to a flatter CV restitution.

3.4.1 The MRI-based electromechanical model of the human ventricles

In this study, we present a strongly-coupled MRI-based model of human cardiac electromechanics. This new model incorporates reconstructions of human ventricular geometry and fiber orientation from MR and DTMR images, which allows for simulation of realistic ventricular deformation during arrhythmias. The circulatory model to which it is coupled is adapted for the human ventricles, enabling accurate representation of hemodynamic changes during arrhythmia. The implementation of strong coupling in our electromechanical model allows for the dynamic inclusion of the effect of MEF in the electrical component since a mechanical solution step was performed following every fifth electrical solution step; this allows for a more accurate simulation of the effect of MEF compared to what has been done previously, where a mechanical solution step followed every 100 electrical solution steps (37). This is the first electromechanical model to incorporate MEF in this manner. The simulations performed using this model in the present study represent a comprehensive evaluation of the electromechanical behavior of the human ventricles in VF and of the effect of SAC opening on arrhythmia stability.

3.4.2 Alteration of cellular electrophysiological properties by MEF

Recruitment of non-selective cation SAC results in prolongation of APD with a crossover during systole, where the early phase of repolarization is shortened and the late phase prolonged (6, 7). Opening of potassium-conducting SAC causes repolarization during systole and results in APD shortening (9). Thus, the combined electrophysiological effect of the opening of the two different SACs can vary depending on the degree of expression of non-selective cation SAC and potassium-conducting SAC

in myocardial tissue; experimental observations have shown both prolongation (7, 39, 57) and shortening of APD or monophasic action potential (58, 59).

Single cell behavior in our models is consistent with this experimental data, as SAC opening with V_{SAC} at -60mV, which represented a higher degree of expression of potassium-conducting SAC, produced shortening of APD. SAC opening with V_{SAC} at -10mV, which represented a higher degree of expression of non-selective cation SAC, resulted in APD prolongation with a crossover and elevation of resting potential. Different conductances have been reported for SAC as well (5); we showed that the degree of lengthening or shortening of APD is affected by SAC conductance. Since recruitment of SAC with different reversal potentials and conductances leads to different electrophysiological changes in cardiac myocytes, it was important to incorporate different degrees of expression of the two types of SAC when examining the whole-heart behavior, extending the findings of an earlier study (37).

3.4.3 Effects of MEF on CV

While examining the dependence of CV on strain was not the subject of this study, this relationship affected the dependence of the CV restitution on MEF, and thus indirectly spiral wave behavior in the model. Previous studies have shown that for a wide range of pacing cycle lengths, the CV can exhibit biphasic; constant; increasing; and decreasing relationship with respect to strain (see review (15)). Our results are consistent with these seemingly disparate findings: we found that CV displays different relationships with respect to stretch depending on pacing cycle length, g_{SAC}, and V_{SAC}. Opening of SAC with V_{SAC} of -10mV resulted in independence of CV on stretch for low

values of g_{SAC} and in a decrease in CV with the increase in stretch for large values of g_{SAC} at all pacing cycle lengths. For low values of g_{SAC}, opening of SAC with V_{SAC} of -10mV produced a small inward I_{SAC} during repolarization, which did not lead to large elevation in the resting membrane potential and thus did not inactivate Na channels and reduce CV. For large values of g_{SAC}, recruitment of SAC with V_{SAC} of -10mV resulted in a larger I_{SAC}, which was sufficient to inactivate Na channels and thus slow conduction. Recruitment of SAC with V_{SAC} of -60mV resulted in the increase in CV with increasing stretch at short pacing cycle lengths (400ms and below) and in a CV unaltered with stretch at long pacing cycle lengths (between 400 and 1000ms) for all values of g_{SAC}. Opening of SAC with V_{SAC} of -60mV shortened APD and thus increased DI. At short pacing cycle lengths, the increase in DI led to a better recovery from refractoriness and thus increased CV, whereas at large pacing cycle lengths, there was already a full recovery from refractoriness without SAC opening and thus the increase in DI did not increase CV.

3.4.4 Effect of SAC recruitment on scroll wave stability

There has been a significant body of research on the determinants of scroll wave stability. APD and CV restitution relationships have been found to be two main determinants of scroll wave stability; a flat APD or CV restitution curve was shown to lead to stable scroll waves, whereas a steep APD or CV restitution relation gives rise to scroll wave breakup (54, 60, 61). Studies concerning determinants of scroll wave stability have mainly been electrophysiological without taking into account the effect of mechanical contraction of the ventricles on scroll wave stability. However, heterogeneity

in strain throughout the ventricles, especially during VF, leads to heterogeneous MEF via SAC opening, which affects scroll wave stability. Since experimental studies require contraction to be blocked to reduce movement artifacts from optical mapping recording (62), realistic modeling offers a means to explore how mechanical contraction of the ventricles affects scroll wave stability via MEF.

We showed that opening of SAC with V_{SAC} of -60mV diminished scroll wave breakup by flattening the APD restitution curve. Our findings are consistent with experimental results on scroll wave stability in the presence of the drug D600 (a calcium channel blocker at low concentrations), which caused acceleration of repolarization and shortening of APD, effects similar to those of SAC opening with V_{SAC} of -60mV: D600 similarly promoted scroll wave stability by flattening the APD restitution curve (17).

We also demonstrated that opening of SAC with V_{SAC} of -10mV partially inhibits scroll wave breakup at low values of g_{SAC} by flattening the CV restitution relation in regions of high stretch. Previous studies have shown that slowing of scroll wave rotation leads to stabilization of scroll waves (41, 63, 64); the mechanism is that the period of rotation and thus the diastolic interval increase, resulting in the operational regime being in the less steep part of the APD restitution curve (63, 64). This indirect suppression of scroll wave breakup is also present in our simulation results, as Na channels were inactivated with opening of SAC with V_{SAC} of -10mV and thus scroll wave rotation was slowed.

For large values of g_{SAC}, recruitment of SAC with V_{SAC} of -10mV did not diminish the likelihood of scroll wave breakup because Na channel inactivation in regions of large stretch as a result of SAC opening led to conduction block and thus scroll wave breakup,

which counteracted the increased scroll wave stability due to a flatter CV restitution. This is consistent with results obtained by Keldermann et al.'s (37). Since Keldermann et al. evaluated the effect of large SAC conductances only, the destabilizing effect of SAC opening on scroll waves was the dominant mechanism. The study by Kuijpers et al. (65) demonstrated that in the atria, Na channel inactivation as a result of SAC opening leads to functional block, thereby terminating arrhythmias. The fact that Na channel inactivation as a result of SAC opening led to scroll wave breakup in the ventricles, whereas in atria it led to termination of arrhythmias might be due to the fact that atria have less tissue for propagation compared to the ventricles. Atria, unlike the ventricles, may not be able to support an alternative pathway circumventing the conduction block that is long enough, compared to the wavelength, to result in the establishment of a sustained reentry.

The results of the study demonstrate the possible therapeutic potential of SAC recruitment during VF, indicating that clinical strategies could be devised to minimize scroll wave breakup. For instance, gene therapy could be designed and tested to increase the expression of potassium-conducting SACs, so that g_{SAC} would be increased while V_{SAC} is brought closer to the myocyte resting potential. This will bring SACs to a regime that maximizes the suppression of scroll wave breakup.

3.4.5 Study limitations

Previous experiments have shown that SAC conductance can be a function of strain rate (2, 66). However, this limitation would not greatly affect our results since it was previously shown that regions with larger strains were associated with larger strain rates

(67). SAC was assumed to be uniformly distributed in the ventricles. Such assumption was made due to lack of experimental studies on this subject.

Chapter 4

Efficient preloading of the ventricles by a properly timed atrial contraction underlies stroke work improvement in the acute response to cardiac resynchronization therapy[2]

4.1 Introduction

Heart failure is a major cause of morbidity and mortality (12), contributing significantly to global health expenditure. A large number of heart failure patients exhibit a LBBB type of electrical activation. In such patients, the LV is activated through the septum from the RV, resulting in a delayed onset of LV contraction relative to that of the RV (13). CRT, which employs bi-ventricular pacing to re-coordinate the contraction of the heart, has been demonstrated to be a valuable therapeutic option for such patients (14). Even though CRT has been shown to improve heart failure symptoms and reduce

[2]This chapter was published in ref. 68. Hu Y, Gurev V, Constantino J, Trayanova N. Efficient preloading of the ventricles by a properly timed atrial contraction underlies stroke work improvement in the acute response to cardiac resynchronization therapy. Heart Rhythm. 2013;10(12):1800-6. Epub 2013/08/10.and is reprinted with permission from Elsevier.

Contributions other than the author's: Dr. Viatcheslav Gurev and Dr. Jason Constantino co-developed the model with the author.

hospitalization for most of the patients, one third of them fail to benefit from the therapy (14), reflecting an incomplete understanding of the mechanisms underlying the response to CRT. Gaining a better understanding of these mechanisms will help optimize the delivery of CRT so that the benefit of the therapy is extended to a larger patient population.

CRT typically involves implantation of three leads, one into RA, and two in the RV and LV, respectively. The two ventricular electrodes provide stimuli simultaneously to elicit a synchronous contraction. Optimization of the pacing time interval between activating the RA and the subsequent activation of both ventricles (AV delay) has been shown to additionally improve the acute hemodynamic response of the heart (69). Heart failure patients often exhibit mitral regurgitation as a result of ventricular dilation and increased chamber sphericity (70). CRT has also been shown to acutely reduce mitral regurgitation severity in the DHF ventricles (70-72) by increasing the transmitral pressure gradient (the systolic LV-LA pressure difference) (70) and diminishing the dyssynchrony of papillary muscle contraction (71, 72). Overall, the acute response of the DHF ventricles to CRT is thus believed to be due to 3 main mechanisms: resynchronization of ventricular contraction, efficient preloading of the ventricles by a properly timed atrial contraction, and reduced mitral regurgitation (18).

The acute response to CRT is manifested by an augmentation in stroke work (19). However, the contribution of each of the three mechanisms to stroke work improvement during the acute response to CRT has not been quantified and therefore, the predominant mechanism underlying this improvement has not been identified. Currently, it is difficult to isolate and quantify the contribution of each of the three mechanisms to CRT-induced

stroke work increase through experimental methods (73, 74). Therefore, a computational approach was undertaken in this study. A MRI-based electromechanical model of the DHF ventricles was developed to determine the contribution of each of the three proposed mechanisms to CRT-induced acute stroke work augmentation and to identify the predominant mechanism.

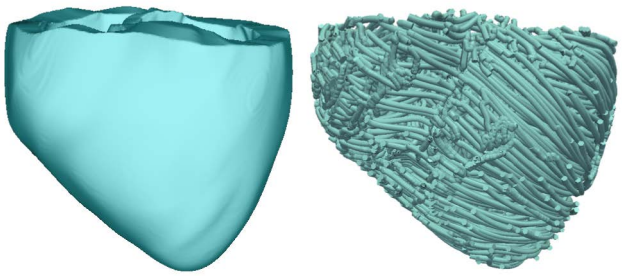

Figure 4.1: Geometry (left) and fiber orientation (right) of the DHF canine ventricular model.

4.2 Methods

4.2.1 MRI-based electromechanical model of the DHF canine ventricles

To achieve the goals of this study, we employed an MRI-based electromechanical model of the DHF canine ventricles (Fig. 4.1) developed previously by our group (22). The model and the advancements implemented in it for the present research are described briefly below. The ventricular geometry and fiber-sheet architecture of the model were constructed from high-resolution MR and DTMR images of DHF canine ventricles. The model consisted of coupled electrical and mechanical components, and a lumped-parameter representation of the circulatory system. Mathematical description of the

electrical component of the model involved the use of the monodomain representation of cardiac tissue; the ventricular mechanics component was based on the continuum mechanics equations, with the myocardium assumed to be orthotropic, hyperelastic nearly-incompressible material (21, 27, 28).

For computational tractability, the electrical and mechanical components of the electromechanical model were weakly coupled. The local electrical activation times calculated from the electrical component of the model determined the instants when the Ca transient, which served as an input into the Rice et al. myofilament model (26) in the mechanics component of the model, was initiated at the Gaussian points of each mechanical mesh element. The electrical component of the ventricular electromechanical model employed the Luo–Rudy dynamic model, LRd (25) to represent membrane kinetics; generic mammalian membrane kinetics models, such as LRd, are often used in whole-heart electromechanical models (67, 75), LRd is considered to be of medium-to-low complexity and is thus a reasonable trade-off in large-scale electromechanical simulations.

The formulation of the Ca transient in the myofilament model was modified to reflect abnormal Ca handling associated with DHF (76), namely the peak Ca amplitude was reduced by 40% and the time for decay of the Ca transient to its half-maximal value was increased by 40% from the corresponding values in the normal canine ventricles; the latter values can be found in Provost et al. (46). Modified parameters in the representation of the Ca transient in Rice et al. model include:

$\tau_1 = 0.035\text{s}$

$\tau_2 = 0.17s$

$Ca_{amplitude} = 1.0\mu M$

$Ca_{peak} = 0.7\mu M$

The modified formulation of the Ca transient in Rice et al. model is as follows:

$$\beta = \left(\frac{\tau_1}{\tau_2}^{-1/\left(\frac{\tau_1}{\tau_2}-1\right)} - \frac{\tau_1}{\tau_2}^{-1/\left(1-\frac{\tau_2}{\tau_1}\right)}\right) \quad (4.1)$$

$$Ca_t = \begin{cases} Ca_{diastolic} & \text{for } t \le t_{start} \\ min\left\{\left(\frac{Ca_{amplitude}-Ca_{diastolic}}{\beta}\right)\left(e^{-\frac{t-t_{start}}{\tau_1}} - e^{-\frac{t-t_{start}}{\tau_2}}\right) + Ca_{diastolic}, Ca_{peak}\right\} & \text{for } t > t_{start} \end{cases} \quad (4.2)$$

Furthermore, the values of the scaling factor for tension, of the crossbridge attachment rate constant to the first strongly-bound state, and of the scaling factor for all crossbridge cycling rates were adjusted to represent behavior in the canine ventricles; these were set to 205, $5000s^{-1}$ and 0.4, respectively, so that ejection fraction, LV peak pressure, and maximal rise in LV pressure matched values observed experimentally in failing canine ventricles (77). Additionally, the elastance of the atria in the lumped-parameter model of the circulatory system (78) was increased fourfold so that atrial contraction accounted for 10% of ventricular filling, as reported for the failing canine ventricles (79).

Mitral regurgitation was represented in the model of the circulatory system by allowing for backward flow from LV to the LA when LV pressure was higher than LA pressure. Regurgitant flow was formulated as the pressure difference between LV and LA divided by the product of mitral valve resistance and the scaling factor for mitral valve resistance.

$$Q_{mitral} = \begin{cases} \frac{P_{LA}-P_{LV}}{R_{mitral}} & P_{LA} \geq P_{LV} \\ \frac{P_{LA}-P_{LV}}{R_{mitral} \times MR_{factor}} & P_{LA} \leq P_{LV} \end{cases} \quad \text{.....(4.3)}$$

where Q_{mitral} is the mitral flow rate, P_{LA} and P_{LV} are the LA and LV pressures, R_{mitral} is the mitral valve resistance, and MR_{factor} is the scaling factor for mitral valve resistance

The scaling factor for mitral valve resistance was set to 500 so that the mitral regurgitant fraction, the ratio of the regurgitant volume to mitral inflow volume, was 31% in the model of the DHF ventricles, consistent with the mitral regurgitant fraction measured experimentally in failing ventricles (71).

To simulate LBBB activation of the canine ventricles, the RV endocardial surface of the ventricles was stimulated at a basic pacing cycle length of 500ms (77) at discrete locations as if the electrical activation was emanating from the activation of the corresponding branch of the Purkinje network; the locations and timings were based on experimental findings (80). LBBB was simulated with an AV delay of 140ms, as recorded in DHF canine ventricles (77).

4.2.2 CRT simulation

The model of the DHF ventricles described above was subjected to CRT, modeled as follows: RA pacing was represented by the onset of atrial contraction via initiating the activation function for atrial elastance in the model of the circulatory system; at a certain AV delay, the ventricles were paced simultaneously from the RV apex and the LV lateral wall.

Stroke work was calculated by integrating the area within the pressure-volume loop. Stroke work improvement (or worsening) following CRT was defined as the percentage

increase (or decrease) of stroke work as a result of CRT relative to that in the DHF ventricles. Previous research has demonstrated that a physiologically meaningful CRT response is associated with a minimum of 15% stroke work improvement (19).

Simulation protocol (I): Quantifying stroke work improvement as a result of resynchronization of ventricular contraction alone

Experimental evidence has demonstrated that both ventricular filling following atrial contraction and mitral regurgitation reduction affect ventricular hemodynamics (81, 82). Therefore, to quantify how much stroke work improvement resulted from CRT-induced resynchronization of ventricular contraction alone, DHF ventricular activation and CRT were simulated without accounting for atrial contraction and in the absence of mitral regurgitation (the DHF model in this case is only that of LBBB activation). This was achieved by setting the activation function for atrial elastance and the scaling factor for mitral valve resistance to 0 and infinity, respectively, in the lumped-parameter model of the circulatory system. The stroke work following CRT was compared to that under LBBB activation to determine whether there is a stroke work improvement due to resynchronization of ventricular contraction alone.

Simulation protocol (II): Quantifying stroke work improvement as a result of efficient preloading of the ventricles by a properly timed atrial contraction

Clinical and experimental studies have found that varying the pacing time interval between RA activation and ventricular activation (AV delay) in CRT affects the preloading of the ventricles and thus ventricular hemodynamics performance (69, 81, 83,

84). To understand how the duration of the AV delay imposed by the device affects the preloading of the ventricles and thus stroke work improvement following CRT, the DHF canine ventricular model with mitral regurgitation eliminated from it was employed in this protocol; device-imposed AV delays were varied between 0 and 140ms. This allowed us to determine the **additional** CRT stroke work improvement contributed by the efficient preloading of the ventricles due to a properly timed atrial contraction, over the baseline stroke work improvement resulting from resynchronization of ventricular contraction alone.

Simulation protocol (III): Quantifying stroke work improvement as a result of mitral regurgitation reduction by CRT

CRT has been shown to reduce mitral regurgitation to a different extent (71), which would then result in different changes in stroke work (85). Accordingly, we employed the original DHF canine ventricular model to simulate different degrees of CRT-induced mitral regurgitation reduction in this study: the scaling factor for mitral valve resistance was chosen (values are presented in Table 4.1) so that mitral regurgitant fraction either remained at 31% or was reduced to 15% or 0% as a result of CRT. The AV delay that gave rise to the maximal stroke work improvement as determined from simulation protocol II was used in the CRT simulations.

4.3 Results

Figure 4.2 portrays the 3D distribution maps of fiber strain at end-diastole, mid-systole and late-systole in the DHF canine ventricular model. Dyssynchronous activation

is evident by the fact that when the septal wall contracted, the LV lateral wall was pre-stretched at mid-systole and the lateral wall shortened at late-systole. These 3D deformation patterns are consistent with those found experimentally in DHF ventricles (86).

Table 4.1: Stroke work improvement in simulation protocol III.

Stroke work for LBBB activation (kPa*mL)	Mitral regurgitant ratio after CRT (%)	Scaling factor for mitral valve resistance	Stroke work after CRT (kPa*mL)	Stroke work improvement (%)
163.2	31	710	231.6	41.9
	15	1670	209.5	28.4
	0	infinity	190.6	16.8

The results from simulation protocol I show that resynchronization of ventricular contraction, which resulted in a reduction of total activation time from 151ms in the DHF ventricles to 109ms following CRT, led to only 8.7% stroke work improvement, from 137.2 to 149.1 kPa*mL. Since stroke work improvement only above 15% is considered meaningful (19), our simulations concluded that resynchronization of ventricular contraction (i.e. reduction of total activation time) alone does not give rise to meaningful stroke work improvement.

The simulation results from protocol II demonstrated that stroke work improvement increased when AV delay decreased from 140ms to 40ms; when AV delay further shortened reaching 0ms, stroke work improvement decreased (Table 4.2). The maximum

stroke work improvement was 40.5% achieved at an optimal AV delay of 40ms (Table 4.2). These results demonstrate that optimizing AV delay is critical to achieving a significant stroke work improvement.

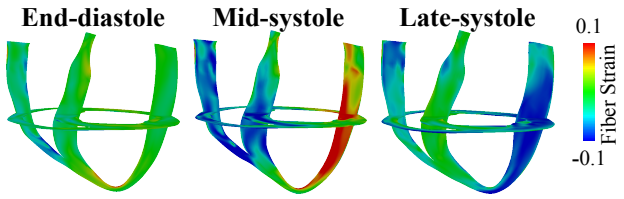

Figure 4.2: Distribution of fiber strain at three different time instants in the failing canine ventricular model with simulated LBBB electrical activation.

Since resynchronization of ventricular contraction did not result in marked stroke work improvement, while optimizing AV delay led to a significant stroke work improvement, it is possible that marked stroke work could be obtained through optimizing AV delay alone, without resynchronization of ventricular contraction (i.e. without reduction in total activation time). To test this hypothesis, we employed the DHF model from simulation protocol II; instead of pacing from RA and both ventricles for CRT, we only paced from RA and varied the time interval between RA pacing and LBBB electrical activation in the ventricles from 0 to 140ms. Stroke work improvement peaked at 29.8% when AV delay was 40ms (Table 4.2). This demonstrates that optimizing AV delay alone leads to significant stroke work improvement. Adding the 29.8% stroke work improvement by optimizing AV delay alone to the stroke work improvement resulting solely from resynchronization of ventricular contraction (8.7%) amounts to a total stroke

Table 4.2: Stroke work improvement for various AV delays.

AV delay (ms)	140	110	70	40	0
Stroke work for CRT where only the RA was paced (kPa*mL)	135.7*	152.9	170.9	176.2*	167.2*
Stroke work improvement for CRT where only the RA was paced (%)	0.0	12.7	25.9	29.8	23.2
Stroke work for CRT simulations in protocol II (kPa*mL)	156.6	174.1	189.5	190.6	173.4
Stroke work improvement for CRT simulations in protocol II (%)	15.4	28.3	39.6	40.5	27.8

* Cases corresponding to traces presented in Figure 5.3.

work improvement of 38.5%, which is similar to that obtained under simulation protocol II with an AV delay of 40ms (40.5%). This shows that resynchronization of ventricular contraction (reduction in total activation time) contributed to the increased stroke work improvement, but not significantly.

To understand how optimizing AV delay alone, without resynchronization of ventricular contraction, increases stroke work improvement significantly, we examined the pressure and volume changes obtained in simulations in which we only paced the RA and changed the time interval between RA pacing and LBBB electrical activation in the ventricles (Fig. 4.3). Comparing LV pressures from simulations with AV delays of 40ms and 140ms, it can be seen that when AV delay was short, atrial contraction occurred when LV pressure was lower. As a result, the pressure against which LV filling by atrial contraction occurred was lower with an AV delay of 40ms. This led to an increase in LV end-diastolic volume and a larger stroke work improvement when AV delay was shortened from 140ms to 40ms (Fig. 4.3B, Table 4.2). However, when AV delay was shortened further to 0ms, even though the diastolic LV pressure was lower than that for AV delay of 40ms, LV filling time decreased by 20ms (Fig. 4.3A). As a result, the LV end-diastolic volume and thus the stroke work improvement were smaller than when AV delay was 40ms (Fig. 4.3B, Table 4.2). Therefore, by optimizing AV delay, preloading of the ventricles became more efficient and stroke work improvement increased. The mechanism underlying significant stroke work improvement following CRT was thus the efficient preloading of the ventricles by a properly timed atrial contraction.

Our simulations found that diminution of mitral regurgitation associated with CRT did not lead to additional stroke work improvement; it actually caused a worsening in stroke work. Indeed, the results from simulation protocol III showed that if CRT did not reduce mitral regurgitation, stroke work improvement was 41.9%. However, if CRT reduced mitral regurgitation, stroke work improvement became less than that; decreasing

mitral regurgitant ratio from 31% to 15% and 0% by CRT gave rise to only 28.4% and 16.8% stroke work improvement, respectively (Table 4.1).

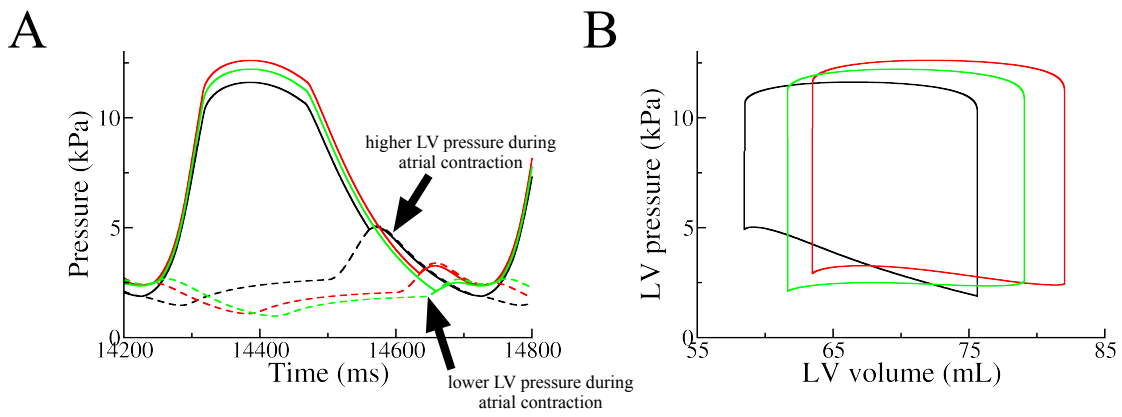

Figure 4.3: (A): LA (broken lines) and LV (solid lines) pressures and **(B):** pressure-volume loops from the simulations in which we only paced the RA and varied the time interval, 140 (black), 40 (red) and 0 ms (green), between RA pacing and LBBB electrical activation in the ventricles.

As shown in Table 4.3, in the DHF ventricular model from protocol III, 7.6mL and 16.5mL of blood were ejected by the LV into the LA and aorta, respectively. Stroke work for the DHF ventricles was 163.2kPa*mL: the work done by the LV to eject blood into the LA and the aorta were -17.3kPa*mL (the reason the work done by the LV to eject blood into the LA was negative was due to the fact that the mitral inflow volume was more than the regurgitant volume) and 180.5kPa*mL, respectively. If CRT reduced

Table 4.3: Diminution of mitral regurgitation by CRT led to stroke work worsening.

	Ejection of blood by the LV into the LA (mL)	Ejection of blood by the LV into the aorta (mL)	Work done by the LV to eject blood into the LA (mJ)	Work done by the LV to eject blood into the aorta (mJ)	Stroke work for the DHF ventricles (mJ)
DHF	7.6	16.5	-17.3	180.5	163.2
CRT	0.0	19	-49.7	240.2	190.6

mitral regurgitant ratio to 0%, 19mL of blood was ejected by the LV into the aorta. Stroke work for the ventricles following CRT was 190.6kPa*mL: the work done by the LV to eject blood into the LA and aorta were -49.7kPa*mL and 240.2kPa*mL, respectively. Therefore, the 27.4kPa*mL (190.6kPa*mL-163.2kPa*mL) CRT-induced stroke work increase was due to 59.7kPa*mL (240.2kPa*mL-180.5kPa*mL) more work done by the LV to eject blood into the aorta but 32.4kPa*mL (-49.7kPa*mL-(-17.2kPa*mL)) less work done to eject blood into the LA.

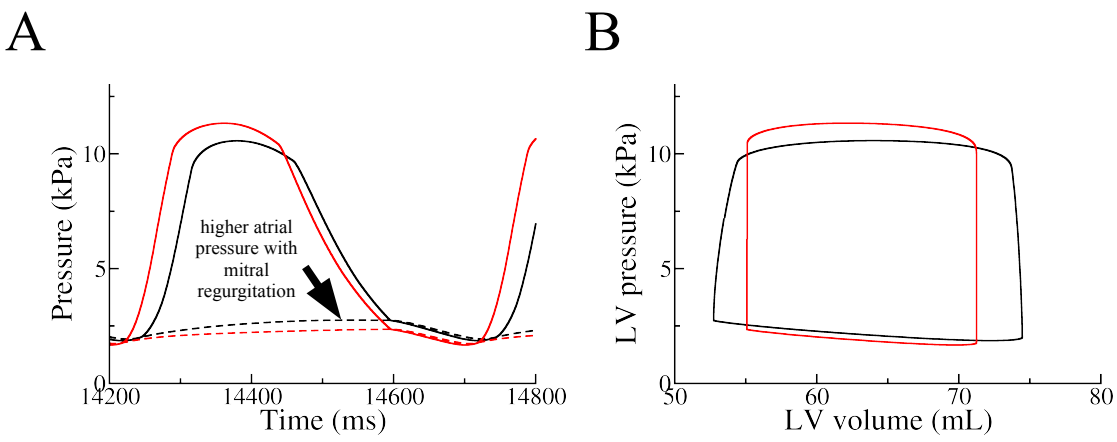

Figure 4.4: (A): LA (broken line) and LV (solid line) pressures and **(B):** pressure-volume loops from the LBBB and CRT simulations using the model from protocol III with atrial contraction eliminated.

Since efficient preloading of the ventricles by a properly timed atrial contraction results in significant stroke work changes in the acute response of CRT, atrial contraction was eliminated from the DHF model to dissect the mechanism by which mitral regurgitation decrease following CRT led to stroke work worsening. The scaling factor for mitral valve resistance was set to infinity so that mitral regurgitant ratio was reduced to 0% in CRT. LV (solid lines) and LA (broken lines) pressures from both LBBB activation (black) and CRT (red) simulations are plotted in Figure 4.4A. Mitral regurgitation in the DHF ventricles gave rise to elevation of atrial pressure (Fig. 4.4A) due to blood leaking back into the LA during ventricular systole. The elevated atrial pressure was then transmitted to the LV during filling so that LV end-diastolic volume was increased by 3mL (Fig. 4.4B). The net result was an increase in stroke volume and

stroke work with mitral regurgitation (Fig. 4.4B). Thus diminution of mitral regurgitation by CRT led to stroke work worsening.

4.4 Discussion

This study identified the predominant mechanism underlying stroke work augmentation in the acute response of CRT by employing an MRI-based anatomically accurate 3D model of the DHF canine ventricular electromechanics. For the first time, the contribution of each of the three mechanisms, namely resynchronization of ventricular contraction, reduction of mitral regurgitation, and efficient preloading of the ventricles by a properly timed atrial contraction, to stroke work improvement was quantified and the mechanisms identified. Significant findings of this study include:

1. Resynchronization of ventricular contraction alone did not result in significant stroke work improvement.
2. Efficient preloading of the ventricles by a properly timed atrial contraction was the predominant mechanism underlying stroke work improvement.
3. Stroke work improvement peaked at an intermediate AV delay, as it allowed ventricular filling by atrial contraction to occur at a low diastolic LV pressure but also provided adequate time for ventricular filling before ventricular contraction.
4. Diminution of mitral regurgitation by CRT led to stroke work worsening instead of improvement.

4.4.1 The acute response to CRT

In this paper we demonstrated that resynchronization of ventricular contraction did not improve stroke work significantly in our canine model of DHF ventricles, which is consistent with the results from previous computational (87) and clinical studies (88). In fact, the predominant mechanism underlying stroke work improvement was efficient preloading of LV by a properly timed atrial contraction, in agreement with clinical data (88). However, other clinical results has demonstrated that resynchronization of ventricular contraction led to significant stroke work improvement (89). Since there is large interindividual variability in the hemodynamics of the DHF ventricles in CRT clinical studies (90), it is possible that resynchronization of ventricular contraction contributes to varying degrees of stroke work improvement in different patients.

Our simulation results demonstrated that when the AV delay was in the intermediate range, stroke work improvement was larger than when the AV delay was short or long. If mitral regurgitation reduction by CRT was small, stroke work augmentation was more than that if mitral regurgitation reduction by CRT was large. Therefore, we surmise that the reason why some patients do not respond to CRT, specifically do not register a significant stroke work improvement following CRT might be due to the fact that they had a non-optimal device-imposed AV delay or/and large degree of mitral regurgitation reduction as a result of CRT.

4.4.2 Optimal AV delay

We demonstrated that the AV delay needed to achieve maximum stroke work improvement in the acute response of CRT had an intermediate value (40ms in the tested

range of 0-140ms). Clinical and experimental studies have found that the optimal AV delay in terms of hemodynamic metrics other than stroke work, such as maximal cardiac output (81), maximal rise in LV increase (69, 83, 84), aortic systolic pressure increase (83) and pulse pressure improvement (83) also have an intermediate value. The reason why these hemodynamic metrics were reduced at short and long AV delays was that with a short AV delay, atrial contraction occurred simultaneously with ventricular contraction, resulting in inefficient ventricular filling (81), consistent with our analysis; when the AV delay was too long, preloading of the LV was impaired due to diastolic mitral regurgitation (81). We showed that with a long AV delay, especially at relatively fast pacing rates (2Hz), preloading of the LV was impaired due to the high diastolic pressure against which atrial contraction occurred, which made ventricular filling by atrial contraction inefficient. It is possible that with a longer pacing cycle length, there would be more time for ventricular relaxation. Therefore, we expect that the LV pressure against which LV filling by atrial contraction occurs would not be significantly higher with a longer AV delay (140ms) compared to that at a shorter AV delay (40ms), as found here. As a result, preloading of the ventricles would not be as significantly impaired as in this study, and therefore, stroke work improvement would be larger at a longer AV delay. The contribution of efficient preloading of the ventricles by a properly timed atrial contraction to stroke work improvement could thus be less with a larger pacing cycle length.

4.4.3 Mitral regurgitation reduction due to CRT

CRT has been shown to acutely reduce mitral regurgitation severity in DHF patients (70-72). Two mechanisms have been proposed to explain how mitral regurgitation was

reduced by CRT: CRT resulted in an increase in transmitral pressure gradient (the systolic LV-LA pressure difference), which effectively counteracted the increased tethering forces in heart failure that impaired mitral valve competence (70); and CRT diminished dyssynchrony of papillary muscle contraction in DHF, which led to reduced mitral regurgitation (71, 72). Our results demonstrate that mitral regurgitation gave rise to higher LA pressure, end-diastolic volume, stroke volume, and stroke work, in agreement with clinical and experimental results (82, 85, 91, 92). Inducing mitral regurgitation in dogs has been shown to result in increased LA pressure, end-diastolic volume, stroke volume, and stroke work (82, 85). End-diastolic volume, stroke volume and stroke work were higher in patients with mitral regurgitation than in the control subjects (91) or in patients after surgical treatment of mitral valve disease (92).

4.4.4 Clinical significance

Our findings indicate that in order to maximize, clinically, the acute CRT hemodynamic response in terms of improvement in stroke work, the best strategy would be to focus on optimizing device-imposed AV delay. Our simulations indicated that an intermediate AV delay (between 0ms and the AV delay in LBBB activation) would be optimal.

4.4.5 Limitations

The model for mitral regurgitation in this study is relatively simple compared to existing models (93). However, there is no reason to expect that incorporating a more complex model for mitral regurgitation would alter the main conclusions of this

simulation study regarding the predominant mechanism underlying stroke work improvement in the acute response of CRT.

4.5 Conclusion

In the present study, we quantified the contribution of each of the three mechanisms hypothesized to underlie stroke work improvement in the acute CRT response, namely resynchronization of ventricular contraction, improved preloading of the ventricles by a properly timed atrial contraction, and mitral regurgitation reduction. The predominant mechanism underlying significant stroke work improvement was found to be improved preloading of the ventricles by a properly timed atrial contraction.

Chapter 5

Optimizing CRT to minimize ATP consumption heterogeneity throughout the left ventricle: A simulation analysis using a canine heart failure model[3]

5.1 Introduction

Heart failure is a major cause of morbidity and mortality (12), contributing significantly to global health expenditure. A large number of heart failure patients exhibit contractile dyssynchrony due to LBBB; in these patients, the contraction of the LV is delayed compared to that of the RV (13, 95). CRT, the administering of biventricular pacing to the ventricles to re-coordinate contraction, has proven to be an effective therapy for DHF patients (14, 96, 97).

In DHF patients, as a result of contractile dyssynchrony, the myocardial blood flow (a measure of myocardial workload) and oxygen consumption is higher in the LV lateral wall compared to the septum (98). Over the long term, the LV lateral wall mass increases to a greater extent relative to the septal mass, i.e. an asymmetry in the hypertrophic response develops (99). CRT has been demonstrated to lead to the restoration of relative

[3] This chapter was published in ref. 94. Hu Y, Gurev V, Constantino J, Trayanova N. Optimizing CRT to Minimize ATP Consumption Heterogeneity Throughout the Left Ventricle: A Simulation Analysis Using a Canine Heart Failure Model. Ibid. 2014.and is reprinted with permission from Elsevier.

Contributions other than the author's: Dr. Viatcheslav Gurev and Dr. Jason Constantino co-developed the model with the author.

homogeneity in oxygen consumption throughout the LV by increasing the oxygen consumption of the septum and decreasing that of the lateral wall (98, 100). Homogeneous oxygen consumption, which indicates uniform distribution of myocardial workload, throughout the LV is important for long-term reverse remodeling of the ventricles as it eliminates the asymmetry in hypertrophy resulting from LBBB (99).

Consequentially, an important consideration in the quest to improve the long-term efficacy of CRT for DHF patients is that oxygen (or ATP) consumption heterogeneity throughout the LV be minimized. However, thus far research into CRT has not addressed this issue -- previous studies have mainly focused on improving the acute response of CRT (19). Indeed, only the optimal LV pacing sites that give rise to acute hemodynamic improvements, such as stroke work increase, have been identified (19). It therefore remains unclear whether there exist LV pacing sites that could both improve the acute hemodynamic response and result in a relatively homogeneity of ATP consumption throughout the LV, thus maximizing both short-term and long-term benefits of CRT.

The goal of the present study was to address this issue. We aimed to demonstrate the feasibility of optimizing CRT pacing locations to achieve minimal ATP consumption heterogeneity throughout the LV while simultaneously maximizing hemodynamics improvement in the DHF canine ventricles. An MRI-based electromechanical model of the DHF canine ventricles previously developed by us was augmented and used to achieve the study goals.

5.2 Materials and Methods

We employed an MRI-based electromechanical model of the DHF canine ventricles (Fig. 5.1A) developed previously by our group (22, 68). The model, as previously published, is briefly described in Appendix A. For the present research, we implemented further advancements in the model to enable us to determine the ATP consumption throughout the LV at a high spatiotemporal resolution. Detailed description of these new model developments is also provided in Appendix A.

5.2.1 CRT Simulation protocol

Currently, in a routine clinical CRT device implantation procedure, LV pacing sites are accessed via the coronary sinus and are thus epicardial (101). Accordingly, the model of the DHF ventricles was subjected to bi-ventricular CRT, in which the ventricles were paced simultaneously from the RV apex and an epicardial location in the LV. This protocol is similar to the CRT protocol described in our recent publication (68). The parameters chosen in the CRT model, such as CRT AV delay and pacing rate are

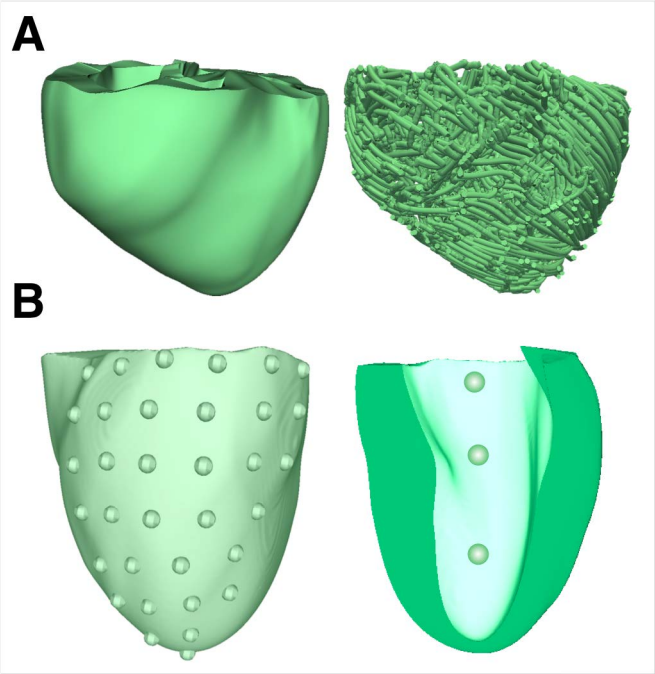

Figure 5.1: (A): Geometry (left) and fiber orientation (right) of the DHF canine ventricular model. **(B):** Distribution of 34 evenly spaced LV epicardial pacing sites (left). The view was adjusted to show only the LV lateral wall, as most of the LV pacing sites were located on the lateral wall. Distribution of the 3 LV endocardial pacing sites (right) in a visual rendering of the LV endocardium.

provided in Appendix A. To determine the optimal epicardial LV CRT pacing locations that result in minimum ATP consumption heterogeneity throughout the LV while simultaneously maximizing stroke work improvement, 34 evenly spaced LV epicardial pacing sites were tested (Fig. 5.1B, left). For each LV pacing site, maps of the distribution of ATP_cT, the ATP consumption per myosin head (see Appendix A for

detail), were constructed, and a single ATP_cT heterogeneity index heterogeneity index, ATPCTHI, calculated (see Appendix A for detail).

In addition, we also simulated bi-ventricular CRT with endocardial LV placement to gain insight into whether it could lead to different improvements in ATPCTHI and stroke work as compared to epicardial LV placement. Three LV endocardial pacing sites were tested: one basal, one apical and one midway between apex and base (Fig. 5.1B, right). Improvements in both ATPCTHI and stroke work were calculated for each of them. In all CRT simulations, the position of the RV pacing lead remained the same.

5.2.2 Data analysis

For each bi-ventricular CRT simulation (corresponding to each of the 34 epicardial LV and the 3 endocardial LV pacing locations), the degree of heterogeneity in ATP consumption throughout the LV and the improvement in ATPCTHI was determined. These novel calculations are described in detail in Appendix A. Additionally, the optimal LV pacing site(s), both epicardial (among 34 locations) and endocardial (among 3 locations) that led to maximal improvement in stroke work were calculated as described in our previous publication (68) and briefly presented in Appendix A. Finally, the LV pacing sites that achieve maximal improvement in both ATPCTHI and stroke work were identified.

5.3 Results

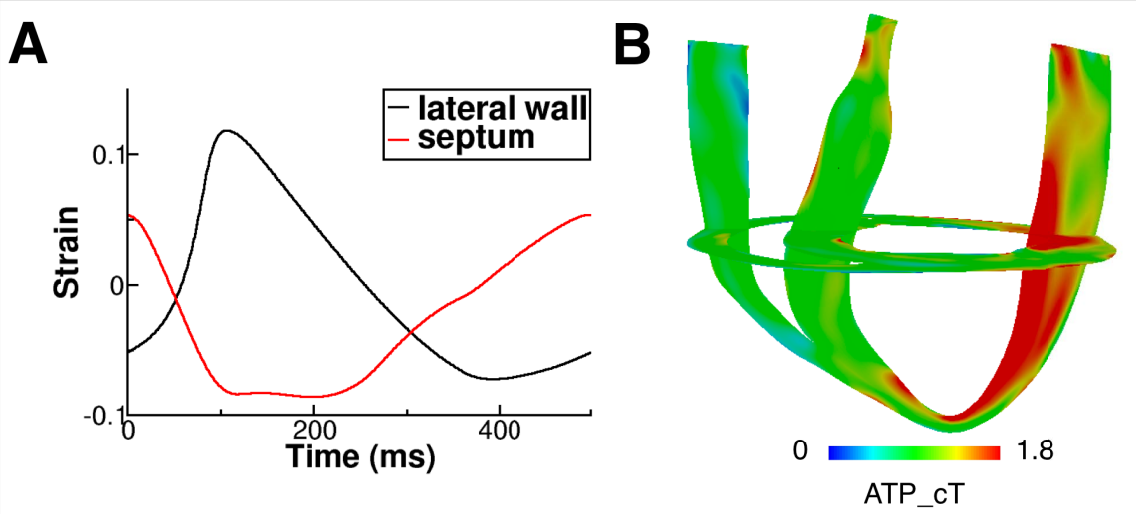

Figure 5.2: (A): Strain profiles over one pacing cycle from representative sites, one on the LV lateral wall and another on the septum in the DHF canine ventricular model with simulated LBBB electrical activation. **(B):** 3D distribution of ATP_cT in the DHF canine ventricles.

Figure 5.2A presents contraction in the model of the DHF canine ventricles. The black and red lines are the strain profiles over one pacing cycle from representative sites, one on the LV lateral wall and another on the septum. It can be seen that contraction is dyssynchronous: the septal wall shortened while the LV lateral wall was pre-stretched; the lateral wall contraction was delayed relative to that of the septum. These strain profiles are consistent with experimental recordings in the DHF ventricles (86) and with the simulated strain maps in our previous publication (68). Figure 5.2B shows the 3D distribution of ATP_cT in the DHF canine ventricles: ATP_cT was larger in the LV lateral wall compared to the septum, resulting in an ATPCTHI of 0.327.

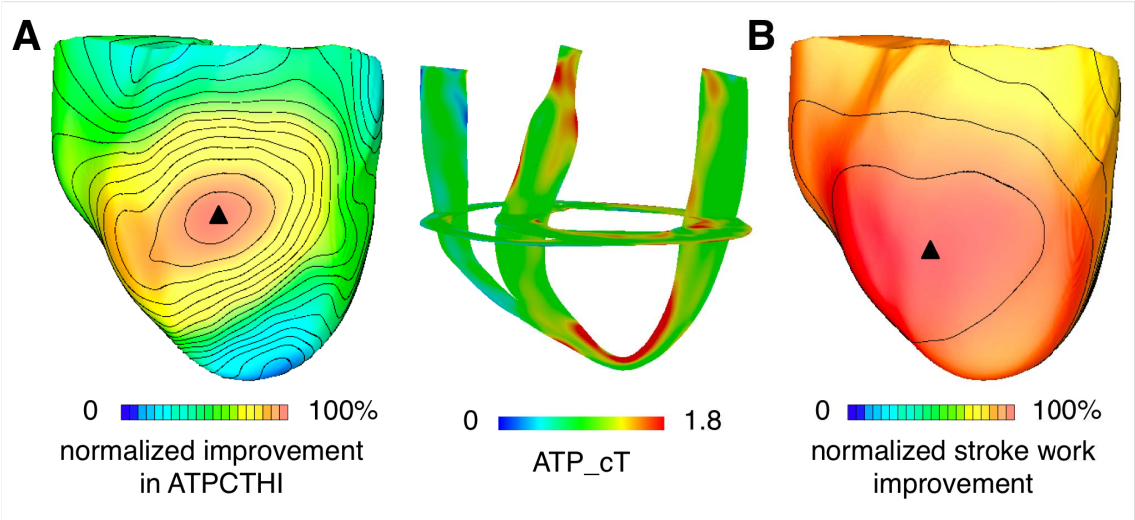

Figure 5.3: (A): Distribution of improvement in ATPCTHI over all epicardial LV pacing sites for biventricular CRT (left). Improvement in ATPCTHI was normalized with respect to the maximal improvement in ATPCTHI; the value of the maximal amount of improvement in ATPCTHI was determined among the 34 CRT simulation results (corresponding to the 34 LV epicardial pacing sites). The range 0 to 100% was chosen here for the purpose of comparing isochrones between panels A and B. 3D distribution of ATP_cT in the ventricles following CRT from the epicardial LV site that resulted in maximal improvement in ATPCTHI (right). **(B):** Distribution of stroke work improvement over all epicardial LV pacing sites for biventricular CRT. Stroke work improvement for each of the 34 LV pacing sites was normalized with respect to the maximal stroke work improvement; the value of the maximal stroke work improvement was determined among the 34 sets of CRT simulation results.

Simulations of biventricular CRT were executed to determine the epicardial LV location that resulted in maximum improvement in ATPCTHI following CRT. First, for

all 34 LV CRT locations, ATP_cT maps were constructed. Then, the ATPCTHI values, one for each CRT simulation, were determined. The left image of Fig. 5.3A is a summary plot of the results of all 34 simulations; it presents the distribution of the improvement in ATPCTHI (normalized with respect to the maximal improvement in ATPCTHI, 20%) over all pacing sites. Both apical and basal pacing sites gave rise to small (<10%) improvement in ATPCTHI (i.e. <50% improvement in ATPCTHI normalized with respect to the maximal improvement in ATPCTHI, as seen in Fig. 5.3A, left). The pacing site that resulted in maximal improvement in ATPCTHI was located midway between apex and base, and is marked by the black triangle. CRT from this LV pacing location homogenized ATP_cT between the septum and the lateral wall by increasing septal ATP_cT while decreasing that of the lateral wall (Fig. 5.3A, right), resulting in an ATPCTHI of 0.259.

To provide a reference value, we also calculated ATPCTHI for the failing ventricles in sinus rhythm; the activation patterns corresponding to sinus rhythm, LBBB, and CRT from the optimal pacing site are shown in Figure 5.4. The ATPCTHI in sinus rhythm was 0.268, slightly larger than that (0.259) following CRT from the LV location that resulted in maximal improvement in ATPCTHI.

Simulations of biventricular CRT were then conducted to determine the epicardial LV location that resulted in maximum stroke work improvement. Figure 5.3B is a summary plot of the results of all 34 simulations, each corresponding to one LV site; it shows the distribution of stroke work improvement (normalized with respect to the maximal stroke work improvement, 41%) over all pacing sites. Almost all of the pacing

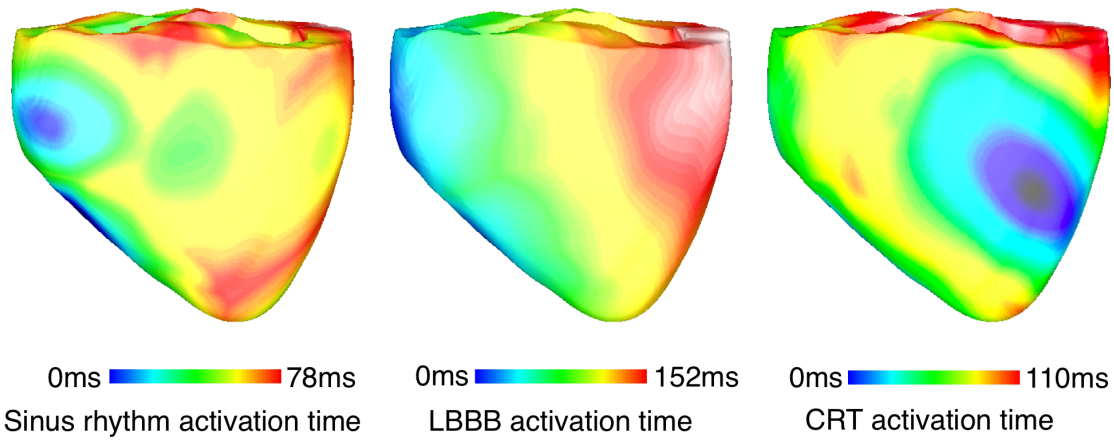

Figure 5.4: Electrical activation pattern in the canine ventricles corresponding to sinus rhythm, LBBB, and CRT from the optimal epicardial LV pacing site.

sites (33 out of 34) led to ≥ 33% stroke work improvement (i.e. ≥ 80% stroke work improvement normalized with respect to the maximal stroke work improvement as seen in Fig. 5.3B). The pacing site that gave rise to the maximal stroke work improvement was located midway between apex and base (marked by the black triangle). The corresponding pressure-volume loop for this CRT location and its comparison to the pressure-volume loop in LBBB are presented in Supplemental Results and Discussion of Appendix A.

The pacing site that resulted in maximal improvement in ATPCTHI was adjacent to the one that led to maximal stroke work improvement and thus, CRT from both LV pacing sites (optimal sites) resulted in maximal or near maximal improvement in both ATPCTHI and stroke work. Figure 5.5 is a plot showing the number of CRT LV pacing

sites that gave rise to improvement above a certain level in both ATPCTHI and stroke work as a function of that level. It shows how close to the maximal improvements in

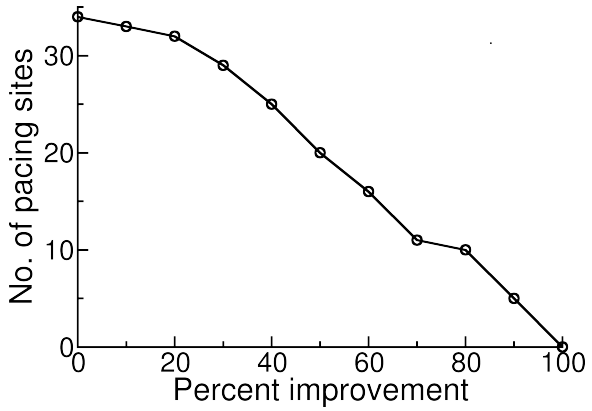

Figure 5.5: The number of CRT LV pacing sites that gave rise to improvement above a certain level in both ATPCTHI and stroke work as a function of that level.

ATPCTHI (20%) and stroke work (41%) the CRT responses from epicardial pacing sites were. For instance, the number of the LV pacing sites that led to improvements in both ATPCTHI and stroke work that were above 40% of the maximum possible was 25. In other words, 25 of the 34 pacing sites resulted in above 8% improvement in ATPCTHI (40% of the maximum 20% improvement in ATPCTHI is 8% improvement) and above 16% stroke work improvement (40% of the maximum 41% improvement in stroke work is 16% stroke work improvement). Similarly, the number of LV pacing sites that led to improvements in both ATPCTHI and stroke work above 80% of maximal was only 10; i.e. 10 LV pacing sites had above 16% improvement in ATPCTHI (80% of the maximum 20% improvement in ATPCTHI is 16% improvement) and above 33% stroke work

improvement (80% of the maximum 41% improvement in stroke work is 33% stroke work improvement).

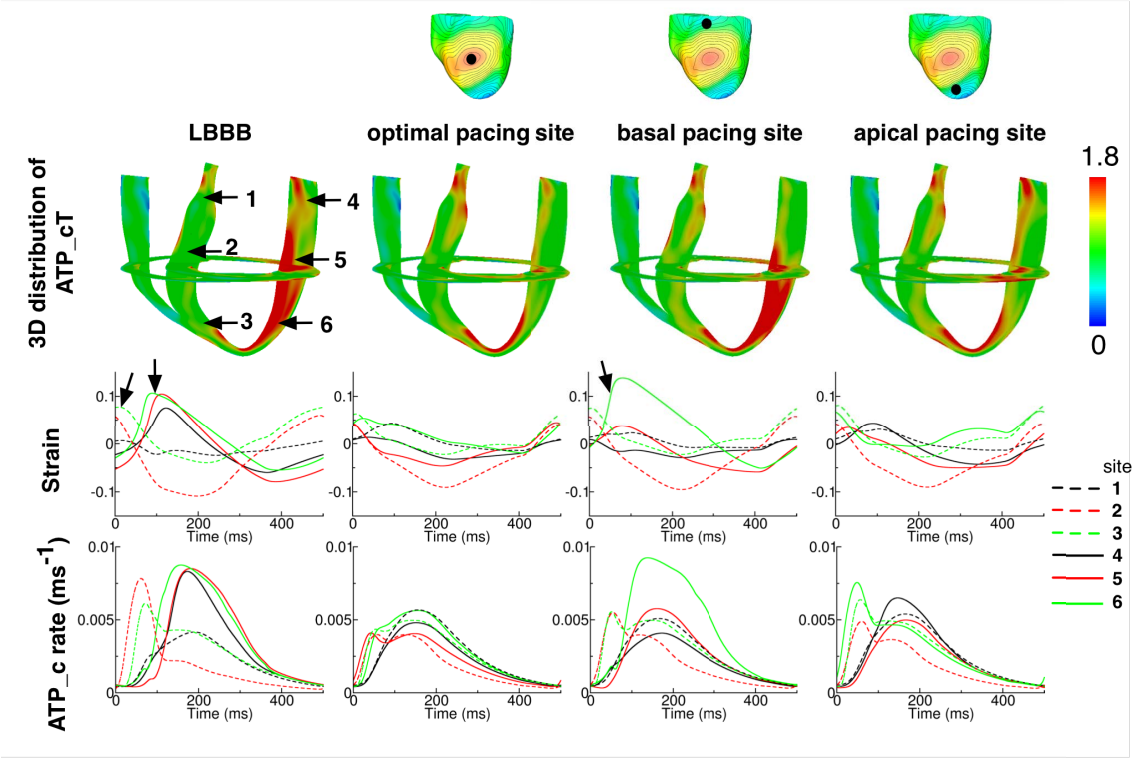

Figure 5.6: 1st row: Canine ventricles. The black dot indicates the location of the CRT epicardial site from which LV was paced. **2nd row:** 3D distribution of ATP_cT in the DHF ventricles and the ventricles following CRT from the epicardial LV pacing sites shown in the 1st row. **3rd and 4th rows:** Strain and ATP_c profile over one representative pacing cycle at six sites (marked by the arrows in the leftmost image in the 2nd row) from DHF ventricles and following CRT from the epicardial LV pacing sites shown in the 1st row.

We also examined the mechanisms by which pacing sites midway between apex and base lead to larger improvement in ATPCTHI. To conduct this analysis, the 3D distributions of ATP_cT in the DHF canine ventricles and following CRT from a basal pacing site, an apical site, and the site that resulted in maximal improvement in ATPCTHI, were compared (Fig. 5.6). Six sites that were on the same longitudinal cross-section (3 on the lateral wall and 3 on the septum, indicated by the arrows in the leftmost image of the 2nd row in Fig. 5.6) were chosen for strain and ATP_c profile analysis. The 3rd and 4th rows of Figure 5.6 present the strain and ATP_c profiles over one representative pacing cycle at each of the six sites in the DHF ventricles and following CRT from the respective LV locations (broken lines are traces from the 3 sites in the septum and solid lines are traces from the 3 sites in the lateral wall). Comparing the strain profiles from the DHF ventricles and following CRT from the LV site that resulted in maximal improvement in ATPCTHI, it can be seen that there is a delay in the lateral wall contraction relative to the septal contraction in the DHF ventricles (onsets of lateral wall and septal contractions are indicated by the arrows). CRT eliminated this dyssynchrony in ventricular contraction, leading to similar ATP_c profiles between septum and lateral wall, and thus significant decrease in ATP_cT heterogeneity throughout the LV and improvement in ATPCTHI (20%).

The basal and apical CRT LV pacing sites shown in Fig. 5.6 resulted in an ATPCTHI of 0.304 and 0.321, respectively; normalized improvements in ATPCTHI were 34% and 8%, respectively. Pacing the LV from the base resulted in the apex contracting after the base, with the apex being pre-stretched (indicated by the arrow, green solid line in the 2nd row panel in Fig. 5.6) while the base was contracting; the pre-stretch was substantial

(14%) as the wall of the apex was thinner than that of the base. This led to fast apical myofiber shortening during the subsequent contraction, as myofibers at the apex shortened to the same degree as those at the base but starting from a fiber pre-stretch of 14%. Consequently, there was higher ATP_c (4^{th} row, basal pacing column) and ATP_cT (2^{nd} row, basal pacing column) at the apex relative to those at the base. Pacing the LV from the apex led to the apex contracting ahead of the base, which resulted in dissimilar ATP_c profiles throughout the LV (4^{th} row, apical pacing column).

Finally, we conducted bi-ventricular endocardial LV CRT simulations. The results demonstrated that the improvements in ATPCTHI were 13% (basal site), 4% (apical site) and 17% (the site midway between apex and base). The maximal improvement in ATPCTHI among the three endocardial pacing sites was 17%, which was close to the maximal improvement in ATPCTHI among the epicardial pacing sites (20%). Apical and basal pacing sites led to smaller improvement in ATPCTHI compared to the pacing site midway between apex and base. The improvements in stroke work were 36% (basal site), 39% (apical site) and 38% (the site midway between apex and base) respectively. Similar to the epicardial pacing sites, all endocardial pacing sites gave rise to stroke work improvement above 33%.

5.4 Discussion

Our study demonstrated the feasibility of determining the optimal LV pacing site for bi-ventricular CRT that achieves simultaneous maximum improvements in ATPCTHI and

stroke work. The results were based on the use of an MRI-based electromechanical model of the DHF canine ventricles. Major findings of the study include:

1. The optimal epicardial LV pacing site for biventricular CRT that resulted in maximal improvement in ATPCTHI was located midway between apex and base, and close to the site that resulted in maximal stroke work improvement.
2. The further the distance on the epicardium from a given LV pacing site to the optimal LV pacing locations, the smaller the improvement in ATPCTHI. Improvement in ATPCTHI decreased much more rapidly with this distance as compared to stroke work improvement.
3. CRT from the optimal epicardial LV pacing sites homogenized ATP_cT throughout the LV by increasing septal ATP_cT and decreasing that of the lateral wall. CRT from epicardial apical or basal sites led to the apex or base contracting ahead of the distant myocardium at base or apex. As a result, CRT from both apical and basal sites gave rise to dissimilar ATP_c profiles throughout the LV, which resulted in heterogeneous ATP_cT in the LV.
4. The location of the endocardial LV CRT pacing site that resulted in maximal improvement in ATPCTHI (among the three sites tested) was in the same general region of the ventricle as the optimal epicardial pacing site.

5.4.1 CRT-induced improvement in ATPCTHI and stroke work

To determine the oxygen consumption throughout the LV, clinical studies had employed ^{11}C-acetate positron emission tomography (98, 100). However, these studies

provided information with low temporal and spatial resolution: myocardial oxygen consumption was measured by the acetate clearance rate at every minute; the LV myocardial wall was divided into four 4 regions (anterior, lateral, inferior and septal wall) and oxygen consumption was quantified for each of them. By using a computational approach to cardiac electromechanics, we were able to evaluate, in 3D and at a high spatiotemporal resolution, the metabolic rate throughout the LV following biventricular CRT, for both epicardial and endocardial LV pacing locations. Our MRI-based 3D electromechanical model of the failing canine ventricles incorporated a myofilament model representing ATP consumption, which made it possible to calculate the dynamic temporal changes in ATP consumption and its heterogeneous distribution throughout the LV. Thus, the LV pacing site that led to maximal improvement in ATPCTHI following CRT could be accurately determined; such CRT optimization could not be achieved in the clinical studies using ^{11}C-acetate positron emission tomography. Analyzing the mechanisms, we found in the present study that the LV pacing site that gave rise to the maximal improvement in ATPCTHI was located midway between apex and base. CRT from non-optimal sites (apical or basal) led to the apex or base contracting ahead of the distant myocardium at base or apex, resulting in dissimilar ATP_c profiles throughout the LV and thus heterogeneous ATP_cT in the LV.

In this study, we demonstrated that stroke work improvement decreased slowly with the distance from the optimal pacing location, which is in agreement with experimental evidence (19, 68). The slow decrease reflected the fact that our model of CRT was tuned to achieve maximum stroke work improvement (see Supplemental Results and

Discussion of Appendix A) as the AV delay used here (70ms) was the value shown to lead to significant stroke work improvement in a canine DHF model (68).

5.4.2 Clinical significance

The results of our study could have important implications for optimizing the clinical procedure of CRT. Our study demonstrated the feasibility of using an image-based simulation approach to determine the optimal LV pacing site for biventricular CRT in the DHF ventricles, a site that achieves simultaneous maximum improvements in ATPCTHI and stroke work. We demonstrated that in the tachycardia-paced canine DHF ventricles (i.e. ventricles without ischemic cardiomyopathy) the optimal LV pacing site was located midway between apex and base (based on extensive simulations of epicardial pacing CRT and a limited number of endocardial CRT simulations). However, we do not expect that in all patients the LV pacing site that maximizes improvements in both ATPCTHI and stroke work would necessarily be at that location. Indeed, clinical studies have shown that there is a significant interindividual variability in the location of the optimal LV pacing site (102-104). The significant interindividual variability in the location of the optimal LV pacing sites found in these clinical studies is due to the fact that a significant percentage of patients had ischemic cardiomyopathy (25%, 56% and 36% in the studies by Asbach et al.(102), Khan et al.(103), and Duckett et al.(104), respectively); the location of scar tissue influences the location of the optimal CRT pacing site (103). The image-based simulation approach to CRT optimization presented here could be applied to each patient heart, building a personalized model (with ischemic cardiomyopathy also

accounted for, should there be any) to be used in determining the optimal LV pacing site (either epi- or endocardial) in a patient-specific manner.

A finding with important clinical implication is that acute hemodynamic response does not necessarily predict long-term CRT outcome, which is consistent with the results from clinical studies (see review(105)). Duckett et al. found that acute response to CRT, as measured by maximal rise in LV pressure, is predictive of long-term response (104). However, this study defined long-term response only in terms of reduction in LV end-systolic volume, which is only one component of reverse remodeling. Elimination of asymmetry in hypertrophy resulting from LBBB, as examined here, is a different, in fact poorly explored, aspect of reverse remodeling by CRT.

5.4.3 Limitations

A limitation in our model is that because of the weak electromechanical coupling in the model we could not represent pacing-induced electro-mechanical remodeling, namely the prolongation of APD in the late-activated myocardial segment as compared to the early-activated myocardial segment found in experimental studies (106, 107); one expects that such electromechanical remodeling might affect the location of the LV pacing site that maximizes improvements in ATPCTHI. As more sophisticated electromechanical models are implemented in the future, the spatial heterogeneity in APD could be taken into account in calculating the optimal pacing site that will result in maximal improvements in ATPCTHI and stroke work following the approach developed

here. Another limitation is that the electromechanical model did not incorporate papillary muscles. It is possible that when modeling advances enough to be able to handle the contribution of papillary muscle, the optimal LV pacing site might be found to be closer to the apex, as found in some experiments (19).

5.5 Conclusion

In the present study, we demonstrated the feasibility of determining the optimal LV pacing site for biventricular CRT that achieves simultaneous maximum improvements in ATPCTHI and stroke work. In the tachycardia-paced DHF canine ventricles these optimal CRT LV pacing sites were located midway between apex and base. Our study suggests an ATP based method to optimize the location of the LV pacing sites for biventricular CRT. Prospective testing would be needed to confirm the feasibility of this method in animal models or patients.

Chapter 6

Overarching Discussion

An in-depth discussion of the specific study finding, implications, and related work is provided in Sections 3.4, 4.4, and 5.4. A brief overarching discussion is given here. This research explored the electromechanical interactions in the heart. First, it was investigated how the recruitment of SAC affects scroll wave stability. Second, the predominant mechanism underlying stroke work improvement in the acute response of CRT was determined. Third, the feasibility of optimizing CRT pacing locations to minimize ATP consumption heterogeneity throughout the LV in the DHF ventricles was demonstrated.

These findings were significant in various ways. Under Specific Aim 1, arrhythmia was induced in human ventricles; it was found that recruitment of SAC affects scroll wave stability differently depending on SAC reversal potential and channel conductance; the mechanisms are also different. The present study was the first comprehensive study to examine the effects of recruitment of SAC with different reversal potentials and conductances on scroll wave stability. The results of the study demonstrate the possible therapeutic potential of SAC recruitment during VF, indicating that clinical strategies could be devised to minimize scroll wave breakup. There is still much unknown about the expression of SAC in ventricular tissue in different patients. It is possible that expression of the two types of SACs, namely non-selective cation SAC and potassium conducting SAC, is heterogeneous throughout the ventricles. Such spatial heterogeneity in SAC

expression throughout the ventricles would complicate how recruitment of SAC affects scroll wave stability. Therefore, it is critical that future studies are conducted to determine SAC expression throughout the ventricles. Under Specific Aim 2, CRT was applied to the DHF canine ventricles. The predominant mechanism underlying stroke work improvement in the acute response of CRT was found to be efficient preloading of the ventricles by a properly timed atrial contraction instead of resynchronization of ventricular contraction. Reduction of mitral regurgitation by CRT led to stroke work worsening. These results indicate that in order to maximize, clinically, the acute hemodynamic response in terms of stroke work, the best strategy would be to focus on optimizing device-imposed AV delay; an intermediate AV delay would be optimal. This study brings up the possibility that resynchronization of ventricular contraction might not be the predominant mechanism underlying stroke work improvement in acute CRT response. However, this study was done using an image-based model of canine ventricles. It is possible that resynchronization of ventricular contraction contributes to greater stroke work improvement in human ventricles given that human ventricles are much larger than canine ventricles. The model in this study did not incorporate DHF induced spatial heterogeneity in electrical and mechanical remodeling, which could have led to greater stroke work improvement as a result of resynchronization of ventricular contraction. Therefore, future studies are needed to investigate whether resynchronization of ventricular contraction leads to larger stroke work improvement in human ventricles compared to canine ventricles and if the spatial heterogeneity in electrical and mechanical remodeling as a result of DHF could have influenced the contribution of resynchronization of ventricular contraction to stroke work improvement in acute CRT

response. It has been shown that there is large interindividual variability in the morphology of pressure-volume loops and hemodynamics among DHF patients. Therefore, future studies should be conducted to determine whether the contribution of resynchronization of ventricular contraction to stroke work improvement in the acute response of CRT differs among patients. Lastly, the model of DHF ventricles did not incorporate representation of papillary muscles. When computational modeling advances enough to incorporate representation of papillary muscles and mitral regurgitation reduction can be simulated in a more realistic manner, a more accurate assessment of the contribution of mitral regurgitation reduction to stroke work improvement can be done. Under Specific Aim 3, CRT was applied to the DHF canine ventricles with the LV pacing site varied among 34 locations on the epicardium. The feasibility of using an image-based simulation approach to determine the optimal LV pacing site in the DHF ventricles that achieves simultaneous maximum improvements in ATPCTHI and stroke work was demonstrated. The results of the study suggest an ATP based method to optimize CRT pacing sites. The image-based simulation approach to CRT optimization presented in the study could be applied to each patient heart, building a personalized model (with ischemic cardiomyopathy also accounted for, should there be any) to be used in determining the optimal LV pacing site in a patient-specific manner. This image-based simulation approach to CRT optimization using an ATP based method needs further testing and validation in both experimental and clinical studies. This study has done extensive simulation of CRT from epicardial pacing sites. Studies can be conducted to optimize endocardial pacing sites, since endocardial pacing has been shown to possibly lead to greater hemodynamic improvements compared to epicardial pacing. Futhermore,

the ATP heterogeneity index can be further improved to better quantify the spatial heterogeneity of ATP consumption throughout the LV by using more advanced statistical techniques such as Moran's I.

Under Specific Aim I, an advanced strongly-coupled electromechanical model of human ventricles was developed. Under Specific Aim II, a sophisticated weakly-coupled electromechanical model of DHF canine ventricles was developed and was further advanced under Specific Aim III to allow us to determine ATP consumption throughout the LV at a high spatiotemporal resolution. Further improvements that can be made to the electromechanical model of the DHF ventricles include incorporating DHF induced electrical and mechanical remodeling, representation of papillary muscles and ischemic cardiomyopathy. These improvements to the electromechanical model of the DHF ventricles will allow more realistic simulations and further optimization of CRT

This research provides insights into the electromechanical interactions in the heart, and will contribute to the development of better treatment for cardiac diseases, specifically cardiac arrhythmias and DHF.

Appendix A

Supplementary Material for Chapter 5[4]

A.1 Supplemental Methods

A. 1.1 Overview of the MRI-based electromechanical model of the DHF ventricles

The ventricular geometry and the three-dimensional arrangement of ventricular myofibers were constructed from high-resolution MR and DTMR images of DHF canine ventricles. The original experimental studies in which the imaging data have been acquired have been previously published (108, 109). The heart failure animal model in these experimental studies (108, 109) was that of a tachycardia pacing-induced heart failure. The imaging data has since been publicly available (http://gforge.icm.jhu.edu/gf/project/dtmri_data_sets). Our electromechanical model consisted of coupled electrical and mechanical components, and a representation of the circulatory system. In the model of the circulatory system, parts (e.g. pulmonic veins) of the system were lumped together and thus compliances were averaged and resistances summed over these parts, as described in (78). The electrical component of the model involved standard methods of wave propagation in the tissue (44). The ventricular

[4] The corresponding study is being published in ref. 94, which is reprinted in Chapter 5. The supplemental material of ref. 94 is reprinted in this appendix.

mechanics component was based on the continuum mechanics equations (21, 27, 28), which treated the myocardium as a continuous medium. The myocardium deformed differently in different directions and it was assumed to be of nearly-incompressible material (21, 27, 28).

To minimize computational effort, the electrical and mechanical components of the electromechanical model were weakly coupled: the local electrical activation times calculated from the electrical component of the model determined the instants when the Ca transient, which served as an input into the Rice et al. myofilament model (26) in the mechanics component of the model, was initiated at the Gauss points of each mechanical mesh element. The electrical component of the ventricular electromechanical model has been extensively described in our previous studies (68, 110).

A.1.2 Myofilament model

The Rice et al. myofilament model (26), as modified in our previous publication (68), was employed in this study. For this study, the myofilament model was further modified so that it could reproduce (Fig. A.1) the experimentally determined relationship between ATP consumption and stress-strain area (the area under the stress-strain curve) (111) and the relationship between ATP consumption and tension at different temperatures (112).

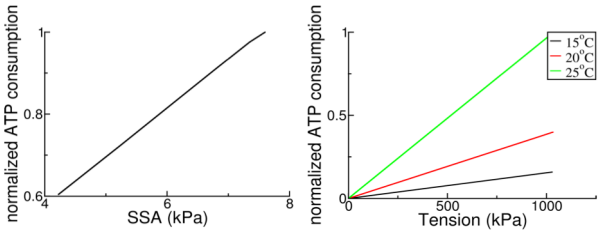

Figure A.1: The myofilament model reproduces experimentally determined relationship between ATP consumption and stress-strain area and the relationship between ATP consumption and tension at different temperatures.

The modifications were implemented by setting the values of the crossbridge detachment rate constant to the permissive conformation state of the regulatory protein, of the scaling constant for the effects of strain on negative shortening velocities, and of the rate constant for Ca binding in the myofilament model to $140s^{-1}$, 1 and $30\mu M^{-1}s^{-1}$, respectively. The value of the scaling factor for tension in the myofilament model was adjusted to 1230 so that ejection fraction, LV peak pressure, and maximal rise in LV pressure matched values observed experimentally in failing canine ventricles (77).

A.1.3 Simulating LBBB activation and CRT in the canine ventricles

To simulate LBBB activation of the canine ventricles, the RV endocardial surface was stimulated at discrete locations as if the electrical activation was emanating from the activation of the corresponding branch of the Purkinje network; the locations and timings were based on experimental findings (80). A pacing cycle length of 500ms was used,

consistent with the pacing rate in DHF canine ventricles in CRT experimental studies (77). LBBB was simulated with an AV delay of 140ms; this AV delay has been measured in the DHF canine ventricles (77). AV delay in the model of LBBB activation was defined as the time interval from the onset of atrial contraction until the start of electrical activation in the ventricles; atrial contraction was represented in the model of the circulatory system using a time-varying elastance model (27, 68).

In each CRT simulation, an AV delay of 70ms was implemented, consistent with the AV delay used in canine CRT protocols (77). CRT AV delay was defined as the time interval from the onset of atrial contraction until the start of biventricular pacing.

A.1.4 Calculating the degree of heterogeneity in ATP consumption throughout the LV

The degree of heterogeneity in ATP consumption throughout the LV was determined by calculating ATP consumption per myosin head (ATP_c) at every Gauss point in the LV mechanical mesh and at every millisecond of the pacing cycle (500ms in duration, from end-diastole of a given cardiac cycle to that of the next). ATP_c calculation involved multiplying the crossbridge detachment rate by the single-overlap fraction of the thick filament and the probability that the crossbridge is in the post-rotated force-generating state in the myofilament model. At each Gauss point in the LV mechanical mesh, ATP_c values calculated at each time instant (every millisecond) of the pacing cycle were then added up to obtain the total ATP_c, ATP_cT (i.e. ATP_c over one pacing

cycle) at that point. ATP_cT thus represented the number of ATP molecules consumed by a single myosin head over one pacing cycle.

$$ATP\_cT\left(\xi_i, \xi_j, \xi_k\right) = \sum_{one\ pacing\ cycle} g_{xbT} XB_{PostR} SOVF_{thick}(x) \quad \text{(A.1)}$$

where g_{xbT} is the crossbridge detachment rate;

XB_{PostR} is the probability that the crossbridge is in the post-rotated force-generating state;

$SOVF_{thick}(x)$ is the single-overlap function for the thick filament;

x is the sarcomere length; and

$ATP\_cT\left(\xi_i, \xi_j, \xi_k\right)$ is the total ATP_c over one pacing cycle at each Gauss point. ξ_i, ξ_j and ξ_k are the local coordinates in Gaussian quadrature and they range from 0 to 1.

For the DHF ventricles and each CRT simulation (corresponding to each of the 34 LV pacing sites), we calculated the ATP_cT heterogeneity index (ATPCTHI), a single value, defined as the dispersion of the ATP_cT across all Gauss points (from the average ATP_cT over all Gauss points) in the LV mechanical mesh.

$$Average\ ATP\_cT = \frac{\sum_{all\ LV\ elements} \sum_i \sum_j \sum_k JW_i W_j W_k ATP\_cT(\xi_i, \xi_j, \xi_k)}{\sum_{all\ LV\ elements} \sum_i \sum_j \sum_k JW_i W_j W_k} \quad \text{(A.2)}$$

$$ATPCTHI = \sqrt{\frac{\sum_{all\ LV\ elements} \sum_i \sum_j \sum_k JW_i W_j W_k (ATP\_cT(\xi_i, \xi_j, \xi_k) - Average\ \ ATP\_cT)^2}{\sum_{all\ LV\ elements} \sum_i \sum_j \sum_k JW_i W_j W_k}} \quad \text{(A.3)}$$

where J is the determinant of the Jacobian of the transformation matrix from local coordinates to global coordinates;

W_i, W_j and W_k are the weights of the Gauss points in ξ_i, ξ_j and ξ_k directions; and

ATPCTHI is the ATP_cT heterogeneity index (ATPCTHI).

Finally, we determined the improvement in ATPCTHI induced by CRT from the given LV pacing site. Improvement in ATPCTHI was defined as the percentage decrease in ATPCTHI as a result of CRT relative to its value in the DHF ventricles.

$$Improvement\ in\ ATPCTHI = \frac{ATPCTHI\ as\ a\ result\ of\ CRT - ATPCTHI\ in\ the\ DHF\ ventricles}{ATPCTHI\ in\ the\ DHF\ ventricles} \quad \text{.....(A.4)}$$

A.1.5 Calculating stroke work improvement

For the DHF ventricles and each CRT simulation (corresponding to each of the 34 LV pacing sites), stroke work was calculated by integrating the area within the pressure-volume loop, as we have done in our previous publication (68). Stroke work improvement for the given pacing site was defined as the percentage increase of stroke work as a result of CRT relative to that in the DHF ventricles.

A.2 Supplemental Results and Discussion: Stroke work improvement in the acute response to CRT

As presented in the main text, stroke work improvement was determined for each of the CRT simulations (34 epicardial LV pacing sites and 3 endocardial LV). Almost all of the epicardial pacing sites (33 out of 34) led to significant (≥ 33%) stroke work improvement, as seen in Fig. 5.3B and discussed in the main text. The slow decrease reflected the fact that our model of CRT was tuned to achieve maximum stroke work improvement i.e. significant stroke work improvement was reached by pacing from a broad area of the LV lateral wall. This tune up was achieved here by setting the AV delay to 70ms, which is the value shown to lead to a significant stroke work improvement in the canine DHF model (68). Indeed, our previous work (68) and a recent experimental study (88) have demonstrated that AV delay optimization was a very important contributor to stroke work improvement following CRT.

The epicardial LV pacing site that resulted in maximal stroke work improvement is marked by the black triangle in Fig. 5.3B. It increased stroke work from 135.7 kPa*mL in the DHF ventricles to 191.3 kPa*mL, as documented by the pressure-volume loops in Fig. A.2. Since the AV delay was 140ms in the DHF ventricles and the pacing cycle length was 500ms (see A.1 Supplementary Methods), atrial contraction occurred when LV was in the process of relaxation and therefore ventricular filling started before the complete relaxation of the LV. Consequently, the pressure at the end of isovolumic relaxation ended up being higher than the end-diastolic pressure. Such pressure-volume relationship has been observed in DHF hearts, such as in Patient 4 and 5 in Dekker et al. (90). The

latter study clearly indicates that there is large interindividual variability in the morphology of pressure-volume loops in CRT clinical studies (90). Future studies are needed to gain a thorough understanding of the hemodynamics in the DHF ventricles prior to and after CRT therapy.

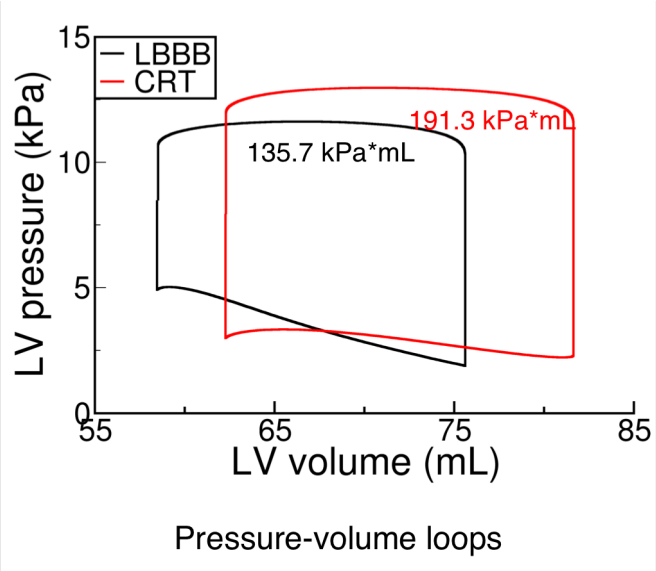

Figure A.2: Pressure-volume loops for the DHF ventricles and the ventricles following CRT from the LV site that resulted in maximal stroke work improvement.

Consistent with findings in our previous research (68), the end-diastolic volume in CRT was higher than that in the DHF ventricles, as seen in Fig. A.2. When the AV delay was shortened from 140ms in the DHF ventricles to 70ms in CRT, atrial contraction occurred when LV was at a more relaxed state and LV pressure was lower. As a result, in CRT, the pressure against which LV filling by atrial contraction occurred was lower than

in the DHF ventricles and LV preloading became more efficient. Consequently, LV end-diastolic volume was larger in CRT and a stronger LV contraction resulted according to Starling's Law.

Bibliography

1. Koller ML, Riccio ML, Gilmour RF, Jr. Dynamic restitution of action potential duration during electrical alternans and ventricular fibrillation. Am J Physiol. 1998;275(5 Pt 2):H1635-42. Epub 1998/11/14.
2. Franz MR, Cima R, Wang D, Profitt D, Kurz R. Electrophysiological effects of myocardial stretch and mechanical determinants of stretch-activated arrhythmias. Circulation. 1992;86(3):968-78.
3. Hu H, Sachs F. Mechanically activated currents in chick heart cells. J Membr Biol. 1996;154(3):205-16.
4. Sachs F. Stretch-activated channels in the heart. In: Kohl P SF, Franz MR, editor. Cardiac Mechano-Electric Feedback and Arrhythmia: From Pipette to Patient: Elsevier; 2004. p. 2-10.
5. Hu H, Sachs F. Stretch-activated ion channels in the heart. J Mol Cell Cardiol. 1997;29(6):1511-23.
6. Zabel M, Koller BS, Sachs F, Franz MR. Stretch-induced voltage changes in the isolated beating heart: importance of the timing of stretch and implications for stretch-activated ion channels. Cardiovascular research. 1996;32(1):120-30.
7. Isenberg G, Kazanski V, Kondratev D, Gallitelli MF, Kiseleva I, Kamkin A. Differential effects of stretch and compression on membrane currents and [Na+]c in ventricular myocytes. Prog Biophys Mol Biol. 2003;82(1-3):43-56.
8. Craelius W, Chen V, el-Sherif N. Stretch activated ion channels in ventricular myocytes. Biosci Rep. 1988;8(5):407-14. Epub 1988/10/01.
9. Van Wagoner DR. Mechanosensitive gating of atrial ATP-sensitive potassium channels. Circ Res. 1993;72(5):973-83. Epub 1993/05/01.
10. Niu W, Sachs F. Dynamic properties of stretch-activated K+ channels in adult rat atrial myocytes. Prog Biophys Mol Biol. 2003;82(1-3):121-35. Epub 2003/05/07.
11. Morris CE. Mechanosensitive ion channels. J Membr Biol. 1990;113(2):93-107. Epub 1990/02/01.
12. Lloyd-Jones D, Adams R, Carnethon M, De Simone G, Ferguson TB, Flegal K, et al. Heart disease and stroke statistics--2009 update: a report from the American Heart Association Statistics Committee and Stroke Statistics Subcommittee. Circulation. 2009;119(3):e21-181. Epub 2008/12/17.
13. Wyndham CR, Smith T, Meeran MK, Mammana R, Levitsky S, Rosen KM. Epicardial activation in patients with left bundle branch block. Circulation. 1980;61(4):696-703. Epub 1980/04/01.
14. Abraham WT, Fisher WG, Smith AL, Delurgio DB, Leon AR, Loh E, et al. Cardiac resynchronization in chronic heart failure. N Engl J Med. 2002;346(24):1845-53. Epub 2002/06/14.

15. McNary TG, Sohn K, Taccardi B, Sachse FB. Experimental and computational studies of strain-conduction velocity relationships in cardiac tissue. Prog Biophys Mol Biol. 2008;97(2-3):383-400. Epub 2008/04/15.
16. Kawase A, Ikeda T, Nakazawa K, Ashihara T, Namba T, Kubota T, et al. Widening of the excitable gap and enlargement of the core of reentry during atrial fibrillation with a pure sodium channel blocker in canine atria. Circulation. 2003;107(6):905-10. Epub 2003/02/20.
17. Wu TJ, Lin SF, Weiss JN, Ting CT, Chen PS. Two types of ventricular fibrillation in isolated rabbit hearts: importance of excitability and action potential duration restitution. Circulation. 2002;106(14):1859-66. Epub 2002/10/03.
18. Abraham WT. Cardiac resynchronization therapy. Prog Cardiovasc Dis. 2006;48(4):232-8. Epub 2006/03/07.
19. Helm RH, Byrne M, Helm PA, Daya SK, Osman NF, Tunin R, et al. Three-dimensional mapping of optimal left ventricular pacing site for cardiac resynchronization. Circulation. 2007;115(8):953-61. Epub 2007/02/14.
20. Vadakkumpadan F, Arevalo H, Prassl AJ, Chen J, Kickinger F, Kohl P, et al. Image-based models of cardiac structure in health and disease. Wiley interdisciplinary reviews Systems biology and medicine. 2010;2(4):489-506. Epub 2010/06/29.
21. Gurev V, Lee T, Constantino J, Arevalo H, Trayanova NA. Models of cardiac electromechanics based on individual hearts imaging data: image-based electromechanical models of the heart. Biomech Model Mechanobiol. 2011;10(3):295-306. Epub 2010/07/01.
22. Constantino J, Hu Y, Trayanova NA. A computational approach to understanding the cardiac electromechanical activation sequence in the normal and failing heart, with translation to the clinical practice of CRT. Prog Biophys Mol Biol. 2012;110(2-3):372-9. Epub 2012/08/14.
23. Hodgkin AL, Huxley AF. A quantitative description of membrane current and its application to conduction and excitation in nerve. The Journal of physiology. 1952;117(4):500-44. Epub 1952/08/01.
24. ten Tusscher KH, Noble D, Noble PJ, Panfilov AV. A model for human ventricular tissue. Am J Physiol Heart Circ Physiol. 2004;286(4):H1573-89. Epub 2003/12/06.
25. Faber GM, Rudy Y. Action potential and contractility changes in [Na(+)](i) overloaded cardiac myocytes: a simulation study. Biophys J. 2000;78(5):2392-404.
26. Rice JJ, Wang F, Bers DM, de Tombe PP. Approximate model of cooperative activation and crossbridge cycling in cardiac muscle using ordinary differential equations. Biophys J. 2008;95(5):2368-90. Epub 2008/02/01.
27. Hu Y, Gurev V, Constantino J, Bayer JD, Trayanova NA. Effects of mechano-electric feedback on scroll wave stability in human ventricular fibrillation. PloS one. 2013;8(4):e60287. Epub 2013/04/11.
28. Gurev V, Constantino J, Rice JJ, Trayanova NA. Distribution of electromechanical delay in the heart: insights from a three-dimensional electromechanical model. Biophys J. 2010;99(3):745-54. Epub 2010/08/05.
29. Kohl P, Hunter P, Noble D. Stretch-induced changes in heart rate and rhythm: clinical observations, experiments and mathematical models. Prog Biophys Mol Biol. 1999;71(1):91-138. Epub 1999/03/10.
30. Kohl P, Ravens U. Cardiac mechano-electric feedback: past, present, and prospect. Prog Biophys Mol Biol. 2003;82(1-3):3-9. Epub 2003/05/07.
31. Xie LH, Sato D, Garfinkel A, Qu Z, Weiss JN. Intracellular Ca alternans: coordinated regulation by sarcoplasmic reticulum release, uptake, and leak. Biophys J. 2008;95(6):3100-10. Epub 2008/06/10.
32. Miragoli M, Gaudesius G, Rohr S. Electrotonic modulation of cardiac impulse conduction by myofibroblasts. Circ Res. 2006;98(6):801-10. Epub 2006/02/18.

33. Baumgarten CM, Clemo HF. Swelling-activated chloride channels in cardiac physiology and pathophysiology. Prog Biophys Mol Biol. 2003;82(1-3):25-42. Epub 2003/05/07.
34. Link MS, Wang PJ, VanderBrink BA, Avelar E, Pandian NG, Maron BJ, et al. Selective activation of the K(+)(ATP) channel is a mechanism by which sudden death is produced by low-energy chest-wall impact (Commotio cordis). Circulation. 1999;100(4):413-8. Epub 1999/07/27.
35. Li W, Kohl P, Trayanova N. Induction of ventricular arrhythmias following mechanical impact: a simulation study in 3D. J Mol Histol. 2004;35(7):679-86. Epub 2004/12/23.
36. Li W, Kohl P, Trayanova N. Myocardial ischemia lowers precordial thump efficacy: an inquiry into mechanisms using three-dimensional simulations. Heart Rhythm. 2006;3(2):179-86. Epub 2006/01/31.
37. Keldermann RH, Nash MP, Gelderblom H, Wang VY, Panfilov AV. Electromechanical wavebreak in a model of the human left ventricle. Am J Physiol Heart Circ Physiol. 2010;299(1):H134-43. Epub 2010/04/20.
38. Panfilov AV, Keldermann RH, Nash MP. Drift and breakup of spiral waves in reaction-diffusion-mechanics systems. Proc Natl Acad Sci U S A. 2007;104(19):7922-6. Epub 2007/05/01.
39. Zeng T, Bett GC, Sachs F. Stretch-activated whole cell currents in adult rat cardiac myocytes. Am J Physiol Heart Circ Physiol. 2000;278(2):H548-57.
40. Moreno JD, Zhu ZI, Yang PC, Bankston JR, Jeng MT, Kang C, et al. A computational model to predict the effects of class I anti-arrhythmic drugs on ventricular rhythms. Science translational medicine. 2011;3(98):98ra83. Epub 2011/09/03.
41. ten Tusscher KH, Panfilov AV. Alternans and spiral breakup in a human ventricular tissue model. Am J Physiol Heart Circ Physiol. 2006;291(3):H1088-100. Epub 2006/03/28.
42. Klingensmith ME, Chen LE, Glasgow SC, Goers TA, Melby SJ. The Washington Manual of Surgery. Klingensmith ME, Chen LE, Glasgow SC, Goers TA, Melby SJ, editors2008.
43. Sharma AD, Bennett TD, Erickson M, Klein GJ, Yee R, Guiraudon G. Right ventricular pressure during ventricular arrhythmias in humans: potential implications for implantable antitachycardia devices. J Am Coll Cardiol. 1990;15(3):648-55. Epub 1990/03/01.
44. Plank G, Zhou L, Greenstein JL, Cortassa S, Winslow RL, O'Rourke B, et al. From mitochondrial ion channels to arrhythmias in the heart: computational techniques to bridge the spatio-temporal scales. Philosophical transactions Series A, Mathematical, physical, and engineering sciences. 2008;366(1879):3381-409. Epub 2008/07/08.
45. Prassl AJ, Kickinger F, Ahammer H, Grau V, Schneider JE, Hofer E, et al. Automatically generated, anatomically accurate meshes for cardiac electrophysiology problems. IEEE transactions on bio-medical engineering. 2009;56(5):1318-30. Epub 2009/02/11.
46. Provost J, Gurev V, Trayanova N, Konofagou EE. Mapping of cardiac electrical activation with electromechanical wave imaging: an in silico-in vivo reciprocity study. Heart Rhythm. 2011;8(5):752-9. Epub 2010/12/28.
47. Vigmond EJ, Hughes M, Plank G, Leon LJ. Computational tools for modeling electrical activity in cardiac tissue. J Electrocardiol. 2003;36 Suppl:69-74. Epub 2004/01/13.
48. Panfilov AV, Keldermann RH, Nash MP. Self-organized pacemakers in a coupled reaction-diffusion-mechanics system. Phys Rev Lett. 2005;95(25):258104. Epub 2005/12/31.
49. Li W, Gurev V, McCulloch AD, Trayanova NA. The role of mechanoelectric feedback in vulnerability to electric shock. Prog Biophys Mol Biol. 2008;97(2-3):461-78. Epub 2008/04/01.
50. Kohl P, Day K, Noble D. Cellular mechanisms of cardiac mechano-electric feedback in a mathematical model. The Canadian journal of cardiology. 1998;14(1):111-9. Epub 1998/03/06.
51. Trayanova N, Li W, Eason J, Kohl P. Effect of stretch-activated channels on defibrillation efficacy. Heart Rhythm. 2004;1(1):67-77. Epub 2005/04/27.
52. Larson C, Dragnev L, Trayanova N. Analysis of electrically induced reentrant circuits in a sheet of myocardium. Ann Biomed Eng. 2003;31(7):768-80.
53. Plonsey R, Barr RC. Bioelectricity. New York: Plenum; 1989.

54. Cherry EM, Fenton FH. Suppression of alternans and conduction blocks despite steep APD restitution: electrotonic, memory, and conduction velocity restitution effects. Am J Physiol Heart Circ Physiol. 2004;286(6):H2332-41. Epub 2004/01/31.
55. Cytrynbaum E, Keener JP. Stability conditions for the traveling pulse: Modifying the restitution hypothesis. Chaos. 2002;12(3):788-99. Epub 2003/06/05.
56. Pollard AE, Burgess MJ, Spitzer KW. Computer simulations of three-dimensional propagation in ventricular myocardium. Effects of intramural fiber rotation and inhomogeneous conductivity on epicardial activation. Circ Res. 1993;72(4):744-56. Epub 1993/04/01.
57. Sung D, Mills RW, Schettler J, Narayan SM, Omens JH, McCulloch AD. Ventricular filling slows epicardial conduction and increases action potential duration in an optical mapping study of the isolated rabbit heart. J Cardiovasc Electrophysiol. 2003;14(7):739-49. Epub 2003/08/22.
58. Eckardt L, Kirchhof P, Monnig G, Breithardt G, Borggrefe M, Haverkamp W. Modification of stretch-induced shortening of repolarization by streptomycin in the isolated rabbit heart. J Cardiovasc Pharmacol. 2000;36(6):711-21.
59. White E, Le Guennec JY, Nigretto JM, Gannier F, Argibay JA, Garnier D. The effects of increasing cell length on auxotonic contractions; membrane potential and intracellular calcium transients in single guinea-pig ventricular myocytes. Exp Physiol. 1993;78(1):65-78. Epub 1993/01/01.
60. Qu Z, Kil J, Xie F, Garfinkel A, Weiss JN. Scroll wave dynamics in a three-dimensional cardiac tissue model: roles of restitution, thickness, and fiber rotation. Biophys J. 2000;78(6):2761-75. Epub 2000/05/29.
61. Weiss JN, Qu Z, Chen PS, Lin SF, Karagueuzian HS, Hayashi H, et al. The dynamics of cardiac fibrillation. Circulation. 2005;112(8):1232-40. Epub 2005/08/24.
62. Girouard SD, Pastore JM, Laurita KR, Gregory KW, Rosenbaum DS. Optical mapping in a new guinea pig model of ventricular tachycardia reveals mechanisms for multiple wavelengths in a single reentrant circuit. Circulation. 1996;93(3):603-13. Epub 1996/02/01.
63. Panfilov AV. Spiral breakup in an array of coupled cells: the role of the intercellular conductance. Physical review letters. 2002;88(11):118101. Epub 2002/03/23.
64. ten Tusscher KH, Panfilov AV. Influence of nonexcitable cells on spiral breakup in two-dimensional and three-dimensional excitable media. Physical review E, Statistical, nonlinear, and soft matter physics. 2003;68(6 Pt 1):062902. Epub 2004/02/03.
65. Kuijpers NH, Potse M, van Dam PM, ten Eikelder HM, Verheule S, Prinzen FW, et al. Mechanoelectrical coupling enhances initiation and affects perpetuation of atrial fibrillation during acute atrial dilation. Heart Rhythm. 2011;8(3):429-36. Epub 2010/11/16.
66. Nishimura S, Kawai Y, Nakajima T, Hosoya Y, Fujita H, Katoh M, et al. Membrane potential of rat ventricular myocytes responds to axial stretch in phase, amplitude and speed-dependent manners. Cardiovascular research. 2006;72(3):403-11.
67. Jie X, Gurev V, Trayanova N. Mechanisms of mechanically induced spontaneous arrhythmias in acute regional ischemia. Circ Res. 2010;106(1):185-92. Epub 2009/11/07.
68. Hu Y, Gurev V, Constantino J, Trayanova N. Efficient preloading of the ventricles by a properly timed atrial contraction underlies stroke work improvement in the acute response to cardiac resynchronization therapy. Heart Rhythm. 2013;10(12):1800-6. Epub 2013/08/10.
69. Kass DA, Chen CH, Curry C, Talbot M, Berger R, Fetics B, et al. Improved left ventricular mechanics from acute VDD pacing in patients with dilated cardiomyopathy and ventricular conduction delay. Circulation. 1999;99(12):1567-73. Epub 1999/03/30.
70. Breithardt OA, Sinha AM, Schwammenthal E, Bidaoui N, Markus KU, Franke A, et al. Acute effects of cardiac resynchronization therapy on functional mitral regurgitation in advanced systolic heart failure. J Am Coll Cardiol. 2003;41(5):765-70. Epub 2003/03/12.

71. Kanzaki H, Bazaz R, Schwartzman D, Dohi K, Sade LE, Gorcsan J, 3rd. A mechanism for immediate reduction in mitral regurgitation after cardiac resynchronization therapy: insights from mechanical activation strain mapping. J Am Coll Cardiol. 2004;44(8):1619-25. Epub 2004/10/19.
72. Ypenburg C, Lancellotti P, Tops LF, Bleeker GB, Holman ER, Pierard LA, et al. Acute effects of initiation and withdrawal of cardiac resynchronization therapy on papillary muscle dyssynchrony and mitral regurgitation. J Am Coll Cardiol. 2007;50(21):2071-7. Epub 2007/11/21.
73. Amat-y-Leon F, Dhingra RC, Wu D, Denes P, Wyndham C, Rosen KM. Catheter mapping of retrograde atrial activation. Observations during ventricular pacing and AV nodal re-entrant paroxysmal tachycardia. Br Heart J. 1976;38(4):355-62. Epub 1976/04/01.
74. Messas E, Pouzet B, Touchot B, Guerrero JL, Vlahakes GJ, Desnos M, et al. Efficacy of chordal cutting to relieve chronic persistent ischemic mitral regurgitation. Circulation. 2003;108 Suppl 1:II111-5. Epub 2003/09/13.
75. Usyk TP, McCulloch AD. Relationship between regional shortening and asynchronous electrical activation in a three-dimensional model of ventricular electromechanics. J Cardiovasc Electrophysiol. 2003;14(10 Suppl):S196-202. Epub 2004/02/06.
76. Beuckelmann DJ, Nabauer M, Erdmann E. Intracellular calcium handling in isolated ventricular myocytes from patients with terminal heart failure. Circulation. 1992;85(3):1046-55. Epub 1992/03/01.
77. Leclercq C, Faris O, Tunin R, Johnson J, Kato R, Evans F, et al. Systolic improvement and mechanical resynchronization does not require electrical synchrony in the dilated failing heart with left bundle-branch block. Circulation. 2002;106(14):1760-3. Epub 2002/10/03.
78. Kerckhoffs RC, Neal ML, Gu Q, Bassingthwaighte JB, Omens JH, McCulloch AD. Coupling of a 3D finite element model of cardiac ventricular mechanics to lumped systems models of the systemic and pulmonic circulation. Ann Biomed Eng. 2007;35(1):1-18. Epub 2006/11/18.
79. Kono T, Sabbah HN, Rosman H, Alam M, Stein PD, Goldstein S. Left atrial contribution to ventricular filling during the course of evolving heart failure. Circulation. 1992;86(4):1317-22. Epub 1992/10/01.
80. Ramanathan C, Jia P, Ghanem R, Ryu K, Rudy Y. Activation and repolarization of the normal human heart under complete physiological conditions. Proc Natl Acad Sci U S A. 2006;103(16):6309-14. Epub 2006/04/12.
81. Nishimura RA, Hayes DL, Holmes DR, Jr., Tajik AJ. Mechanism of hemodynamic improvement by dual-chamber pacing for severe left ventricular dysfunction: an acute Doppler and catheterization hemodynamic study. J Am Coll Cardiol. 1995;25(2):281-8. Epub 1995/02/01.
82. Berko B, Gaasch WH, Tanigawa N, Smith D, Craige E. Disparity between ejection and end-systolic indexes of left ventricular contractility in mitral regurgitation. Circulation. 1987;75(6):1310-9. Epub 1987/06/01.
83. Auricchio A, Stellbrink C, Block M, Sack S, Vogt J, Bakker P, et al. Effect of pacing chamber and atrioventricular delay on acute systolic function of paced patients with congestive heart failure. The Pacing Therapies for Congestive Heart Failure Study Group. The Guidant Congestive Heart Failure Research Group. Circulation. 1999;99(23):2993-3001. Epub 1999/06/15.
84. Vernooy K, Verbeek XA, Cornelussen RN, Dijkman B, Crijns HJ, Arts T, et al. Calculation of effective VV interval facilitates optimization of AV delay and VV interval in cardiac resynchronization therapy. Heart Rhythm. 2007;4(1):75-82. Epub 2007/01/03.
85. Braunwald E, Welch GH, Jr., Sarnoff SJ. Hemodynamic effects of quantitatively varied experimental mitral regurgitation. Circ Res. 1957;5(5):539-45. Epub 1957/09/01.
86. Breithardt OA, Stellbrink C, Herbots L, Claus P, Sinha AM, Bijnens B, et al. Cardiac resynchronization therapy can reverse abnormal myocardial strain distribution in patients with

heart failure and left bundle branch block. J Am Coll Cardiol. 2003;42(3):486-94. Epub 2003/08/09.
87. Kerckhoffs RC, McCulloch AD, Omens JH, Mulligan LJ. Effects of biventricular pacing and scar size in a computational model of the failing heart with left bundle branch block. Medical image analysis. 2009;13(2):362-9. Epub 2008/08/05.
88. Kyriacou A, Pabari PA, Mayet J, Peters NS, Davies DW, Lim PB, et al. Cardiac resynchronization therapy and AV optimization increase myocardial oxygen consumption, but increase cardiac function more than proportionally. International journal of cardiology. 2014;171(2):144-52. Epub 2013/12/18.
89. Hay I, Melenovsky V, Fetics BJ, Judge DP, Kramer A, Spinelli J, et al. Short-term effects of right-left heart sequential cardiac resynchronization in patients with heart failure, chronic atrial fibrillation, and atrioventricular nodal block. Circulation. 2004;110(22):3404-10. Epub 2004/11/24.
90. Dekker AL, Phelps B, Dijkman B, van der Nagel T, van der Veen FH, Geskes GG, et al. Epicardial left ventricular lead placement for cardiac resynchronization therapy: optimal pace site selection with pressure-volume loops. The Journal of thoracic and cardiovascular surgery. 2004;127(6):1641-7. Epub 2004/06/03.
91. Leung DY, Armstrong G, Griffin BP, Thomas JD, Marwick TH. Latent left ventricular dysfunction in patients with mitral regurgitation: feasibility of measuring diminished contractile reserve from a simplified model of noninvasively derived left ventricular pressure-volume loops. Am Heart J. 1999;137(3):427-34. Epub 1999/02/27.
92. Kennedy JW, Doces JG, Stewart DK. Left ventricular function before and following surgical treatment of mitral valve disease. Am Heart J. 1979;97(5):592-8. Epub 1979/05/01.
93. Grimes RY, Levine RA, Walker PG, Yoganathan AP. Dynamics of systolic pulmonary venous flow in mitral regurgitation: mathematical modeling of the pulmonary venous system and atrium. J Am Soc Echocardiogr. 1995;8(5 Pt 1):631-42. Epub 1995/09/01.
94. Hu Y, Gurev V, Constantino J, Trayanova N. Optimizing CRT to Minimize ATP Consumption Heterogeneity Throughout the Left Ventricle: A Simulation Analysis Using a Canine Heart Failure Model. Heart Rhythm. 2014.
95. Grines CL, Bashore TM, Boudoulas H, Olson S, Shafer P, Wooley CF. Functional abnormalities in isolated left bundle branch block. The effect of interventricular asynchrony. Circulation. 1989;79(4):845-53. Epub 1989/04/01.
96. Auricchio A, Stellbrink C, Sack S, Block M, Vogt J, Bakker P, et al. Long-term clinical effect of hemodynamically optimized cardiac resynchronization therapy in patients with heart failure and ventricular conduction delay. J Am Coll Cardiol. 2002;39(12):2026-33. Epub 2002/06/27.
97. Cazeau S, Leclercq C, Lavergne T, Walker S, Varma C, Linde C, et al. Effects of multisite biventricular pacing in patients with heart failure and intraventricular conduction delay. N Engl J Med. 2001;344(12):873-80. Epub 2001/03/22.
98. Lindner O, Vogt J, Kammeier A, Wielepp P, Holzinger J, Baller D, et al. Effect of cardiac resynchronization therapy on global and regional oxygen consumption and myocardial blood flow in patients with non-ischaemic and ischaemic cardiomyopathy. European heart journal. 2005;26(1):70-6. Epub 2004/12/24.
99. Vernooy K, Cornelussen RN, Verbeek XA, Vanagt WY, van Hunnik A, Kuiper M, et al. Cardiac resynchronization therapy cures dyssynchronopathy in canine left bundle-branch block hearts. European heart journal. 2007;28(17):2148-55. Epub 2007/07/06.
100. Lindner O, Sorensen J, Vogt J, Fricke E, Baller D, Horstkotte D, et al. Cardiac efficiency and oxygen consumption measured with 11C-acetate PET after long-term cardiac resynchronization therapy. Journal of nuclear medicine : official publication, Society of Nuclear Medicine. 2006;47(3):378-83. Epub 2006/03/04.

101. Bristow MR, Saxon LA, Boehmer J, Krueger S, Kass DA, De Marco T, et al. Cardiac-resynchronization therapy with or without an implantable defibrillator in advanced chronic heart failure. N Engl J Med. 2004;350(21):2140-50. Epub 2004/05/21.
102. Asbach S, Hartmann M, Wengenmayer T, Graf E, Bode C, Biermann J. Vector selection of a quadripolar left ventricular pacing lead affects acute hemodynamic response to cardiac resynchronization therapy: a randomized cross-over trial. PloS one. 2013;8(6):e67235. Epub 2013/07/05.
103. Khan FZ, Virdee MS, Palmer CR, Pugh PJ, O'Halloran D, Elsik M, et al. Targeted left ventricular lead placement to guide cardiac resynchronization therapy: the TARGET study: a randomized, controlled trial. J Am Coll Cardiol. 2012;59(17):1509-18. Epub 2012/03/13.
104. Duckett SG, Ginks M, Shetty AK, Bostock J, Gill JS, Hamid S, et al. Invasive acute hemodynamic response to guide left ventricular lead implantation predicts chronic remodeling in patients undergoing cardiac resynchronization therapy. J Am Coll Cardiol. 2011;58(11):1128-36. Epub 2011/09/03.
105. Prinzen FW, Auricchio A. The "missing" link between acute hemodynamic effect and clinical response. Journal of cardiovascular translational research. 2012;5(2):188-95. Epub 2011/11/18.
106. Jeyaraj D, Wan X, Ficker E, Stelzer JE, Deschenes I, Liu H, et al. Ionic bases for electrical remodeling of the canine cardiac ventricle. Am J Physiol Heart Circ Physiol. 2013;305(3):H410-9. Epub 2013/05/28.
107. Jeyaraj D, Wilson LD, Zhong J, Flask C, Saffitz JE, Deschenes I, et al. Mechanoelectrical feedback as novel mechanism of cardiac electrical remodeling. Circulation. 2007;115(25):3145-55. Epub 2007/06/15.
108. Helm PA, Tseng HJ, Younes L, McVeigh ER, Winslow RL. Ex vivo 3D diffusion tensor imaging and quantification of cardiac laminar structure. Magnetic resonance in medicine : official journal of the Society of Magnetic Resonance in Medicine / Society of Magnetic Resonance in Medicine. 2005;54(4):850-9. Epub 2005/09/09.
109. Helm PA, Younes L, Beg MF, Ennis DB, Leclercq C, Faris OP, et al. Evidence of structural remodeling in the dyssynchronous failing heart. Circ Res. 2006;98(1):125-32. Epub 2005/12/13.
110. Constantino J, Hu Y, Lardo AC, Trayanova NA. Mechanistic insight into prolonged electromechanical delay in dyssynchronous heart failure: a computational study. Am J Physiol Heart Circ Physiol. 2013;305(8):H1265-73. Epub 2013/08/13.
111. Delhaas T, Arts T, Prinzen FW, Reneman RS. Regional fibre stress-fibre strain area as an estimate of regional blood flow and oxygen demand in the canine heart. The Journal of physiology. 1994;477 (Pt 3):481-96. Epub 1994/06/15.
112. de Tombe PP, Stienen GJ. Impact of temperature on cross-bridge cycling kinetics in rat myocardium. The Journal of physiology. 2007;584(Pt 2):591-600. Epub 2007/08/25.

Vita

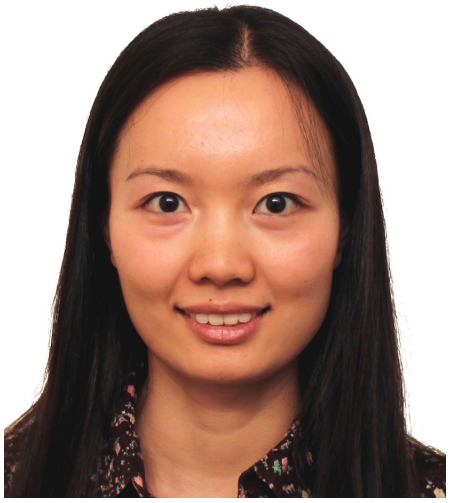

Yuxuan Hu was born on March 15, 1984 in Wuhan, Hubei, China and grew up in Wuhan and Singapore. He received the BSE degree in Biomedical Engineering from Duke University in Durham, NC in 2008 and the MSE degree in Biomedical Engineering from the Johns Hopkins University in 2010. She enrolled in the Biomedical Engineering Ph.D. program at the Johns Hopkins University in 2010. Her research employs computational modeling and focuses on exploring the electromechanical interactions in the heart.

Yuxuan presented her research findings three times at the Annual Scientific Sessions of the Heart Rhythm Society. Yuxuan also presented her research twice at the Gordon Research Conference on Cardiac Arrhythmia Mechanisms. In addition, Yuxuan gave an oral presentation at the American Heart Association Annual Scientific Sessions and an oral presentation at the Biomedical Engineering Society Scientific Sessions. Yuxuan has published a peer-reviewed, first-authored journal article in PLoS One and another two in Heart Rhythm. Overall, Yuxuan has published seven peer-reviewed journal articles and two book chapters.

Yuxuan is interested in both clinical medicine and basic science research and started medical school this year at the Pritzker School of Medicine at the University of Chicago.

Yuxuan has been volunteering extensively during her PhD. She was awarded the Albert Schweitzer Fellowship to implement an electronic medical record system at the Baltimore Rescue Mission Clinic. Yuxuan has a wide variety of interests including ballet, swimming and tennis.

ELSEVIER LICENSE
TERMS AND CONDITIONS

Mar 21, 2014

This is a License Agreement between Yuxuan Hu ("You") and Elsevier ("Elsevier") provided by Copyright Clearance Center ("CCC"). The license consists of your order details, the terms and conditions provided by Elsevier, and the payment terms and conditions.

All payments must be made in full to CCC. For payment instructions, please see information listed at the bottom of this form.

Supplier	Elsevier Limited The Boulevard,Langford Lane Kidlington,Oxford,OX5 1GB,UK
Registered Company Number	1982084
Customer name	Yuxuan Hu
Customer address	5330 S. Blackstone Ave. CHICAGO, IL 60615
License number	3353771234990
License date	Mar 21, 2014
Licensed content publisher	Elsevier
Licensed content publication	Heart Rhythm
Licensed content title	Efficient preloading of the ventricles by a properly timed atrial contraction underlies stroke work improvement in the acute response to cardiac resynchronization therapy
Licensed content author	Yuxuan Hu,Viatcheslav Gurev,Jason Constantino,Natalia Trayanova
Licensed content date	December 2013
Licensed content volume number	10
Licensed content issue number	12
Number of pages	7
Start Page	1800
End Page	1806
Type of Use	reuse in a thesis/dissertation
Intended publisher of new work	other
Portion	full article
Format	electronic
Are you the author of this Elsevier article?	Yes

Will you be translating?	No
Title of your thesis/dissertation	Electromechanical interactions in the heart: a computational study
Expected completion date	Mar 2014
Estimated size (number of pages)	91
Elsevier VAT number	GB 494 6272 12
Permissions price	0.00 USD
VAT/Local Sales Tax	0.00 USD / 0.00 GBP
Total	0.00 USD
Terms and Conditions	

INTRODUCTION

1. The publisher for this copyrighted material is Elsevier. Byclicking "accept" in connection with completing this licensingtransaction, you agree that the following terms and conditions apply to thistransaction (along with the Billing and Payment terms and conditionsestablished by Copyright Clearance Center, Inc. ("CCC"), at the timethat you opened your Rightslink account and that are available at any time at http://myaccount.copyright.com).

GENERAL TERMS

2. Elsevier hereby grants you permission to reproduce the aforementionedmaterial subject to the terms and conditions indicated.

3. Acknowledgement: If any part of the material to be used (for example,figures) has appeared in our publication with credit or acknowledgement toanother source, permission must also be sought from that source. If suchpermission is not obtained then that material may not be included in yourpublication/copies. Suitable acknowledgement to the source must be made, eitheras a footnote or in a reference list at the end of your publication, asfollows:

"Reprinted from Publication title, Vol /edition number, Author(s), Title ofarticle / title of chapter, Pages No., Copyright (Year), with permission fromElsevier [OR APPLICABLE SOCIETY COPYRIGHT OWNER]." Also Lancet special credit -"Reprinted from The Lancet, Vol. number, Author(s), Title of article, PagesNo., Copyright (Year), with permission from Elsevier."

4. Reproduction of this material is confined to the purpose and/or media forwhich permission is hereby given.

5. Altering/Modifying Material: Not Permitted. However figures andillustrations may be altered/adapted minimally to serve your work. Any otherabbreviations, additions, deletions and/or any other alterations shall be madeonly with prior written authorization of Elsevier Ltd. (Please contact Elsevierat permissions@elsevier.com)

6. If the permission fee for the requested use of our material is waived inthis instance, please be advised that your future requests for Elseviermaterials may attract a fee.

7. Reservation of Rights: Publisher reserves all rights not specificallygranted in the combination of (i) the license details provided by you andaccepted in the course of this

licensing transaction, (ii) these terms andconditions and (iii) CCC's Billing and Payment terms and conditions.

8. License Contingent Upon Payment: While you may exercise the rightslicensed immediately upon issuance of the license at the end of the licensingprocess for the transaction, provided that you have disclosed complete andaccurate details of your proposed use, no license is finally effective unlessand until full payment is received from you (either by publisher or by CCC) asprovided in CCC's Billing and Payment terms and conditions. If fullpayment is not received on a timely basis, then any license preliminarilygranted shall be deemed automatically revoked and shall be void as if nevergranted. Further, in the event that you breach any of these terms andconditions or any of CCC's Billing and Payment terms and conditions, thelicense is automatically revoked and shall be void as if never granted. Use of materials as described in a revoked license, as well as any use of thematerials beyond the scope of an unrevoked license, may constitute copyrightinfringement and publisher reserves the right to take any and all action toprotect its copyright in the materials.

9. Warranties: Publisher makes no representations or warranties with respectto the licensed material.

10. Indemnity: You hereby indemnify and agree to hold harmless publisher andCCC, and their respective officers, directors, employees and agents, from andagainst any and all claims arising out of your use of the licensed materialother than as specifically authorized pursuant to this license.

11. No Transfer of License: This license is personal to you and may not besublicensed, assigned, or transferred by you to any other person withoutpublisher's written permission.

12. No Amendment Except in Writing: This license may not be amended exceptin a writing signed by both parties (or, in the case of publisher, by CCC onpublisher's behalf).

13. Objection to Contrary Terms: Publisher hereby objects to any termscontained in any purchase order, acknowledgment, check endorsement or otherwriting prepared by you, which terms are inconsistent with these terms andconditions or CCC's Billing and Payment terms and conditions. These termsand conditions, together with CCC's Billing and Payment terms and conditions(which are incorporated herein), comprise the entire agreement between you andpublisher (and CCC) concerning this licensing transaction. In the eventof any conflict between your obligations established by these terms andconditions and those established by CCC's Billing and Payment terms andconditions, these terms and conditions shall control.

14. Revocation: Elsevier or Copyright Clearance Center may deny thepermissions described in this License at their sole discretion, for any reasonor no reason, with a full refund payable to you. Notice of such denialwill be made using the contact information provided by you. Failure toreceive such notice will not alter or invalidate the denial. In no eventwill Elsevier or Copyright Clearance Center be responsible or liable for anycosts, expenses or damage incurred by you as a result of a denial of yourpermission request, other than a refund of the amount(s) paid by you toElsevier and/or Copyright Clearance Center for denied permissions.

LIMITED LICENSE

The following terms and conditions apply only to specific license types:

15. **Translation**: This permission is granted fornon-exclusive world **English** rights only unless

yourlicense was granted for translation rights. If you licensed translation rightsyou may only translate this content into the languages you requested. Aprofessional translator must perform all translations and reproduce the contentword for word preserving the integrity of the article. If this license is tore-use 1 or 2 figures then permission is granted for non-exclusive world rightsin all languages.

16. **Posting licensed content on any Website**: The followingterms and conditions apply as follows: Licensing material from an Elsevierjournal: All content posted to the web site must maintain the copyright informationline on the bottom of each image; A hyper-text must be included to the Homepageof the journal from which you are licensing at http://www.sciencedirect.com/science/journal/xxxxx orthe Elsevier homepage for books at http://www.elsevier.com; CentralStorage: This license does not include permission for a scanned version of thematerial to be stored in a central repository such as that provided byHeron/XanEdu.

Licensing material from an Elsevier book: A hyper-text link must be includedto the Elsevier homepage at http://www.elsevier.com . Allcontent posted to the web site must maintain the copyright information line onthe bottom of each image.

Posting licensed content on Electronic reserve: In addition to the above the following clausesare applicable: The web site must be password-protected and made available onlyto bona fide students registered on a relevant course. This permission isgranted for 1 year only. You may obtain a new license for future websiteposting.

For journal authors: the following clauses are applicable inaddition to the above: Permission granted is limited to the author acceptedmanuscript version* of your paper.

***Accepted Author Manuscript (AAM) Definition:** An accepted authormanuscript (AAM) is the author's version of the manuscript of an article thathas been accepted for publication and which may include any author-incorporatedchanges suggested through the processes of submission processing, peer review,and editor-author communications. AAMs do not include other publishervalue-added contributions such as copy-editing, formatting, technicalenhancements and (if relevant) pagination.

You are not allowed to download and post the published journal article (whetherPDF or HTML, proof or final version), nor may you scan the printed edition tocreate an electronic version. A hyper-text must be included to the Homepage ofthe journal from which you are licensing at http://www.sciencedirect.com/science/journal/xxxxx. As part of our normal production process, you will receive an e-mail noticewhen your article appears on Elsevier's online service ScienceDirect(www.sciencedirect.com). That e-mail will include the article's Digital ObjectIdentifier (DOI). This number provides the electronic link to the publishedarticle and should be included in the posting of your personal version. We askthat you wait until you receive this e-mail and have the DOI to do any posting.

Posting to a repository: Authorsmay post their AAM immediately to their employer's institutional repository forinternal use only and may make their manuscript publically available after thejournal-specific embargo period has ended.

Please also refer to Elsevier'sArticle Posting Policy for further information.

18. **For book authors** the following clauses are applicable in addition tothe above: Authors

are permitted to place a briefsummary of their work online only.. You are notallowed to download and post the published electronic version of your chapter,nor may you scan the printed edition to create an electronic version. Posting to a repository: Authors arepermitted to post a summary of their chapter only in their institution'srepository.

20. **Thesis/Dissertation**: If your license is for use in athesis/dissertation your thesis may be submitted to your institution in eitherprint or electronic form. Should your thesis be published commercially, pleasereapply for permission. These requirements include permission for the Libraryand Archives of Canada to supply single copies, on demand, of the completethesis and include permission for UMI to supply single copies, on demand, ofthe complete thesis. Should your thesis be published commercially, pleasereapply for permission.

Elsevier Open Access Terms andConditions

Elsevier publishes Open Access articles in both its Open Access journals andvia its Open Access articles option in subscription journals.

Authors publishing in an Open Access journal or who choose to make theirarticle Open Access in an Elsevier subscription journal select one of thefollowing Creative Commons user licenses, which define how a reader may reusetheir work: Creative Commons Attribution License (CC BY), Creative CommonsAttribution – Non Commercial - ShareAlike (CC BY NCSA) and Creative Commons Attribution – Non Commercial – No Derivatives (CC BYNC ND)

Terms & Conditions applicable toall Elsevier Open Access articles:

Any reuse of the article must not represent the author as endorsing theadaptation of the article nor should the article be modified in such a way asto damage the author's honour or reputation.

The author(s) must be appropriately credited.

If any part of the material to be used (for example, figures) has appearedin our publication with credit or acknowledgement to another source it is theresponsibility of the user to ensure their reuse complies with the terms andconditions determined by the rights holder.

Additional Terms & Conditionsapplicable to each Creative Commons user license:

CC BY: You may distribute andcopy the article, create extracts, abstracts, and other revised versions,adaptations or derivative works of or from an article (such as a translation),to include in a collective work (such as an anthology), to text or data minethe article, including for commercial purposes without permission from Elsevier

CC BY NC SA: For non-commercialpurposes you may distribute and copy the article, create extracts, abstractsand other revised versions, adaptations or derivative works of or from anarticle (such as a translation), to include in a collective work (such as ananthology), to text and data mine the article and license new adaptations or creationsunder identical terms without permission from Elsevier

CC BY NC ND: For non-commercialpurposes you may distribute and copy the article and

include it in a collectivework (such as an anthology), provided you do not alter or modify the article,without permission from Elsevier

Any commercial reuse of Open Access articles published with a CC BY NC SA or CC BY NC NDlicense requires permission from Elsevier and will be subject to a fee.

Commercial reuse includes:

- Promotional purposes (advertising or marketing)
- Commercial exploitation (e.g. a product forsale or loan)
- Systematic distribution (for a fee or free ofcharge)

Please refer to Elsevier'sOpen Access Policy for further information.

21. **Other Conditions**:

v1.7

If you would like to pay for this license now, please remit this license along with your payment made payable to "COPYRIGHT CLEARANCE CENTER" otherwise you will be invoiced within 48 hours of the license date. Payment should be in the form of a check or money order referencing your account number and this invoice number RLNK501257628.
Once you receive your invoice for this order, you may pay your invoice by credit card. Please follow instructions provided at that time.

Make Payment To:
Copyright Clearance Center
Dept 001
P.O. Box 843006
Boston, MA 02284-3006

For suggestions or comments regarding this order, contact RightsLink Customer Support: customercare@copyright.com or +1-877-622-5543 (toll free in the US) or +1-978-646-2777.

Gratis licenses (referencing $0 in the Total field) are free. Please retain this printable license for your reference. No payment is required.

ELSEVIER LICENSE
TERMS AND CONDITIONS

Mar 21, 2014

This is a License Agreement between Yuxuan Hu ("You") and Elsevier ("Elsevier") provided by Copyright Clearance Center ("CCC"). The license consists of your order details, the terms and conditions provided by Elsevier, and the payment terms and conditions.

All payments must be made in full to CCC. For payment instructions, please see information listed at the bottom of this form.

Supplier	Elsevier Limited The Boulevard,Langford Lane Kidlington,Oxford,OX5 1GB,UK
Registered Company Number	1982084
Customer name	Yuxuan Hu
Customer address	5330 S. Blackstone Ave. CHICAGO, IL 60615
License number	3353710199776
License date	Mar 21, 2014
Licensed content publisher	Elsevier
Licensed content publication	Heart Rhythm
Licensed content title	Optimizing CRT to Minimize ATP Consumption Heterogeneity Throughout the Left Ventricle: A Simulation Analysis Using a Canine Heart Failure Model
Licensed content author	Hu Yuxuan,Viatcheslav Gurev,Jason Constantino,Natalia Trayanova
Licensed content date	18 March 2014
Licensed content volume number	
Licensed content issue number	
Number of pages	1
Start Page	0
End Page	0
Type of Use	reuse in a thesis/dissertation
Portion	full article
Format	electronic
Are you the author of this Elsevier article?	Yes
Will you be translating?	No

Title of your thesis/dissertation	Electromechanical interactions in the heart: a computational study
Expected completion date	Mar 2014
Estimated size (number of pages)	91
Elsevier VAT number	GB 494 6272 12
Permissions price	0.00 USD
VAT/Local Sales Tax	0.00 USD / 0.00 GBP
Total	0.00 USD
Terms and Conditions	

INTRODUCTION

1. The publisher for this copyrighted material is Elsevier. Byclicking "accept" in connection with completing this licensingtransaction, you agree that the following terms and conditions apply to thistransaction (along with the Billing and Payment terms and conditionsestablished by Copyright Clearance Center, Inc. ("CCC"), at the timethat you opened your Rightslink account and that are available at any time at http://myaccount.copyright.com).

GENERAL TERMS

2. Elsevier hereby grants you permission to reproduce the aforementionedmaterial subject to the terms and conditions indicated.

3. Acknowledgement: If any part of the material to be used (for example,figures) has appeared in our publication with credit or acknowledgement toanother source, permission must also be sought from that source. If suchpermission is not obtained then that material may not be included in yourpublication/copies. Suitable acknowledgement to the source must be made, eitheras a footnote or in a reference list at the end of your publication, asfollows:

"Reprinted from Publication title, Vol /edition number, Author(s), Title ofarticle / title of chapter, Pages No., Copyright (Year), with permission fromElsevier [OR APPLICABLE SOCIETY COPYRIGHT OWNER]." Also Lancet special credit -"Reprinted from The Lancet, Vol. number, Author(s), Title of article, PagesNo., Copyright (Year), with permission from Elsevier."

4. Reproduction of this material is confined to the purpose and/or media forwhich permission is hereby given.

5. Altering/Modifying Material: Not Permitted. However figures andillustrations may be altered/adapted minimally to serve your work. Any otherabbreviations, additions, deletions and/or any other alterations shall be madeonly with prior written authorization of Elsevier Ltd. (Please contact Elsevierat permissions@elsevier.com)

6. If the permission fee for the requested use of our material is waived inthis instance, please be advised that your future requests for Elseviermaterials may attract a fee.

7. Reservation of Rights: Publisher reserves all rights not specificallygranted in the combination of (i) the license details provided by you andaccepted in the course of this licensing transaction, (ii) these terms andconditions and (iii) CCC's Billing and Payment terms

and conditions.

8. License Contingent Upon Payment: While you may exercise the rightslicensed immediately upon issuance of the license at the end of the licensingprocess for the transaction, provided that you have disclosed complete andaccurate details of your proposed use, no license is finally effective unlessand until full payment is received from you (either by publisher or by CCC) asprovided in CCC's Billing and Payment terms and conditions. If fullpayment is not received on a timely basis, then any license preliminarilygranted shall be deemed automatically revoked and shall be void as if nevergranted. Further, in the event that you breach any of these terms andconditions or any of CCC's Billing and Payment terms and conditions, thelicense is automatically revoked and shall be void as if never granted. Use of materials as described in a revoked license, as well as any use of thematerials beyond the scope of an unrevoked license, may constitute copyrightinfringement and publisher reserves the right to take any and all action toprotect its copyright in the materials.

9. Warranties: Publisher makes no representations or warranties with respectto the licensed material.

10. Indemnity: You hereby indemnify and agree to hold harmless publisher andCCC, and their respective officers, directors, employees and agents, from andagainst any and all claims arising out of your use of the licensed materialother than as specifically authorized pursuant to this license.

11. No Transfer of License: This license is personal to you and may not besublicensed, assigned, or transferred by you to any other person withoutpublisher's written permission.

12. No Amendment Except in Writing: This license may not be amended exceptin a writing signed by both parties (or, in the case of publisher, by CCC onpublisher's behalf).

13. Objection to Contrary Terms: Publisher hereby objects to any termscontained in any purchase order, acknowledgment, check endorsement or otherwriting prepared by you, which terms are inconsistent with these terms andconditions or CCC's Billing and Payment terms and conditions. These termsand conditions, together with CCC's Billing and Payment terms and conditions(which are incorporated herein), comprise the entire agreement between you andpublisher (and CCC) concerning this licensing transaction. In the eventof any conflict between your obligations established by these terms andconditions and those established by CCC's Billing and Payment terms andconditions, these terms and conditions shall control.

14. Revocation: Elsevier or Copyright Clearance Center may deny thepermissions described in this License at their sole discretion, for any reasonor no reason, with a full refund payable to you. Notice of such denialwill be made using the contact information provided by you. Failure toreceive such notice will not alter or invalidate the denial. In no eventwill Elsevier or Copyright Clearance Center be responsible or liable for anycosts, expenses or damage incurred by you as a result of a denial of yourpermission request, other than a refund of the amount(s) paid by you toElsevier and/or Copyright Clearance Center for denied permissions.

LIMITED LICENSE

The following terms and conditions apply only to specific license types:

15. **Translation**: This permission is granted fornon-exclusive world **English** rights only unless yourlicense was granted for translation rights. If you licensed translation rightsyou may only

translate this content into the languages you requested. Aprofessional translator must perform all translations and reproduce the contentword for word preserving the integrity of the article. If this license is tore-use 1 or 2 figures then permission is granted for non-exclusive world rightsin all languages.

16. **Posting licensed content on any Website**: The followingterms and conditions apply as follows: Licensing material from an Elsevierjournal: All content posted to the web site must maintain the copyright informationline on the bottom of each image; A hyper-text must be included to the Homepageof the journal from which you are licensing at http://www.sciencedirect.com/science/journal/xxxxx orthe Elsevier homepage for books at http://www.elsevier.com; CentralStorage: This license does not include permission for a scanned version of thematerial to be stored in a central repository such as that provided byHeron/XanEdu.

Licensing material from an Elsevier book: A hyper-text link must be includedto the Elsevier homepage at http://www.elsevier.com . Allcontent posted to the web site must maintain the copyright information line onthe bottom of each image.

Posting licensed content on Electronic reserve: In addition to the above the following clausesare applicable: The web site must be password-protected and made available onlyto bona fide students registered on a relevant course. This permission isgranted for 1 year only. You may obtain a new license for future websiteposting.

For journal authors: the following clauses are applicable inaddition to the above: Permission granted is limited to the author acceptedmanuscript version* of your paper.

***Accepted Author Manuscript (AAM) Definition:** An accepted authormanuscript (AAM) is the author's version of the manuscript of an article thathas been accepted for publication and which may include any author-incorporatedchanges suggested through the processes of submission processing, peer review,and editor-author communications. AAMs do not include other publishervalue-added contributions such as copy-editing, formatting, technicalenhancements and (if relevant) pagination.

You are not allowed to download and post the published journal article (whetherPDF or HTML, proof or final version), nor may you scan the printed edition tocreate an electronic version. A hyper-text must be included to the Homepage ofthe journal from which you are licensing at http://www.sciencedirect.com/science/journal/xxxxx. As part of our normal production process, you will receive an e-mail noticewhen your article appears on Elsevier's online service ScienceDirect(www.sciencedirect.com). That e-mail will include the article's Digital ObjectIdentifier (DOI). This number provides the electronic link to the publishedarticle and should be included in the posting of your personal version. We askthat you wait until you receive this e-mail and have the DOI to do any posting.

Posting to a repository: Authorsmay post their AAM immediately to their employer's institutional repository forinternal use only and may make their manuscript publically available after thejournal-specific embargo period has ended.

Please also refer to Elsevier'sArticle Posting Policy for further information.

18. **For book authors** the following clauses are applicable in addition tothe above: Authors are permitted to place a briefsummary of their work online only.. You are notallowed to

download and post the published electronic version of your chapter,nor may you scan the printed edition to create an electronic version. Posting to a repository: Authors arepermitted to post a summary of their chapter only in their institution'srepository.

20. **Thesis/Dissertation**: If your license is for use in athesis/dissertation your thesis may be submitted to your institution in eitherprint or electronic form. Should your thesis be published commercially, pleasereapply for permission. These requirements include permission for the Libraryand Archives of Canada to supply single copies, on demand, of the completethesis and include permission for UMI to supply single copies, on demand, ofthe complete thesis. Should your thesis be published commercially, pleasereapply for permission.

Elsevier Open Access Terms andConditions

Elsevier publishes Open Access articles in both its Open Access journals andvia its Open Access articles option in subscription journals.

Authors publishing in an Open Access journal or who choose to make theirarticle Open Access in an Elsevier subscription journal select one of thefollowing Creative Commons user licenses, which define how a reader may reusetheir work: Creative Commons Attribution License (CC BY), Creative CommonsAttribution – Non Commercial - ShareAlike (CC BY NCSA) and Creative Commons Attribution – Non Commercial – No Derivatives (CC BYNC ND)

Terms & Conditions applicable toall Elsevier Open Access articles:

Any reuse of the article must not represent the author as endorsing theadaptation of the article nor should the article be modified in such a way asto damage the author's honour or reputation.

The author(s) must be appropriately credited.

If any part of the material to be used (for example, figures) has appearedin our publication with credit or acknowledgement to another source it is theresponsibility of the user to ensure their reuse complies with the terms andconditions determined by the rights holder.

Additional Terms & Conditionsapplicable to each Creative Commons user license:

CC BY: You may distribute andcopy the article, create extracts, abstracts, and other revised versions,adaptations or derivative works of or from an article (such as a translation),to include in a collective work (such as an anthology), to text or data minethe article, including for commercial purposes without permission from Elsevier

CC BY NC SA: For non-commercialpurposes you may distribute and copy the article, create extracts, abstractsand other revised versions, adaptations or derivative works of or from anarticle (such as a translation), to include in a collective work (such as ananthology), to text and data mine the article and license new adaptations or creationsunder identical terms without permission from Elsevier

CC BY NC ND: For non-commercialpurposes you may distribute and copy the article and include it in a collectivework (such as an anthology), provided you do not alter or modify the

article,without permission from Elsevier

Any commercial reuse of Open Access articles published with a CC BY NC SA or CC BY NC NDlicense requires permission from Elsevier and will be subject to a fee.

Commercial reuse includes:

- Promotional purposes (advertising or marketing)
- Commercial exploitation (e.g. a product forsale or loan)
- Systematic distribution (for a fee or free ofcharge)

Please refer to Elsevier'sOpen Access Policy for further information.

21. **Other Conditions**:

v1.7

If you would like to pay for this license now, please remit this license along with your payment made payable to "COPYRIGHT CLEARANCE CENTER" otherwise you will be invoiced within 48 hours of the license date. Payment should be in the form of a check or money order referencing your account number and this invoice number RLNK501257453.
Once you receive your invoice for this order, you may pay your invoice by credit card. Please follow instructions provided at that time.

Make Payment To:
Copyright Clearance Center
Dept 001
P.O. Box 843006
Boston, MA 02284-3006

For suggestions or comments regarding this order, contact RightsLink Customer Support: customercare@copyright.com or +1-877-622-5543 (toll free in the US) or +1-978-646-2777.

Gratis licenses (referencing $0 in the Total field) are free. Please retain this printable license for your reference. No payment is required.